

Twistronics of Kekulé Graphene: Honeycomb and Kagome Flat Bands

Michael G. Scheer¹ and Biao Lian¹

¹*Department of Physics, Princeton University, Princeton, New Jersey 08544, USA*

(Dated: January 9, 2024)

Kekulé-O order in graphene, which has recently been realized experimentally, induces Dirac electron masses on the order of $m \sim 100$ meV. We show that twisted bilayer graphene in which one or both layers have Kekulé-O order exhibits nontrivial flat electronic bands on honeycomb and kagome lattices. When only one layer has Kekulé-O order, there is a parameter regime for which the lowest four bands at charge neutrality form an isolated two-orbital honeycomb lattice model with two flat bands. The bandwidths are minimal at a magic twist angle $\theta \approx 0.7^\circ$ and Dirac mass $m \approx 100$ meV. When both layers have Kekulé-O order, there is a large parameter regime around $\theta \approx 1^\circ$ and $m \gtrsim 100$ meV in which the lowest three valence and conduction bands at charge neutrality each realize isolated kagome lattice models with one flat band, while the next three valence and conduction bands are flat bands on triangular lattices. These flat band systems may provide a new platform for strongly correlated phases of matter.

Moiré systems formed by twisting and stacking two-dimensional (2D) materials often exhibit flat electronic bands. The physics in flat bands is dominated by interactions, so strongly correlated phases often appear. A paradigmatic example is twisted bilayer graphene (TBG) at the magic angle $\theta \approx 1.05^\circ$ [1], which hosts flat bands with fragile topology [2–5] and exhibits a variety of topological and interacting phases including correlated insulators, Chern insulators, and superconductors [6–13]. Similar flat band physics has been observed in moiré systems of multilayer graphene [14–16] and transition metal dichalcogenides [17–21].

An important class of flat bands consists of those arising in tight-binding models due to wavefunction interference effects [22–24]. Examples include the flat bands in the kagome lattice one-orbital and honeycomb lattice two-orbital tight-binding models [25, 26]. Recently, we showed that such flat bands may be realized in moiré heterobilayers of graphene and certain 2D materials with lattice constant approximately $\sqrt{3}$ times that of graphene [27, 28]. This motivates us to search for flat bands in the twistronics of *Kekulé graphene*, which is graphene with a $\sqrt{3} \times \sqrt{3}$ distortion. Kekulé graphene has been experimentally realized via epitaxial growth on a copper surface [29], lithium or calcium intercalation [30–32], or dilute lithium deposition [33, 34]. Kekulé orders have also been observed in graphene in a magnetic field [35, 36] and in correlated insulator phases of TBG [37].

In this paper, we focus specifically on graphene with the Kekulé-O bond order illustrated in Fig. 1(a), which can be realized by intercalation or dilute deposition of lithium [32, 34] and exhibits massive Dirac electrons at low energy [33, 38] (see Supp. Sec. II). We derive a continuum model for TBG with or without Kekulé-O distortions and study two cases: (1) twisted graphene on Kekulé-O graphene (TGKG), in which only one layer has a Kekulé-O distortion, and (2) twisted bilayer Kekulé-O graphene (TBKG), in which both layers have Kekulé-O distortions. Possible realizations of these systems are illustrated in Fig. 1(b).

Despite the Kekulé-O distortion, the moiré unit cell of

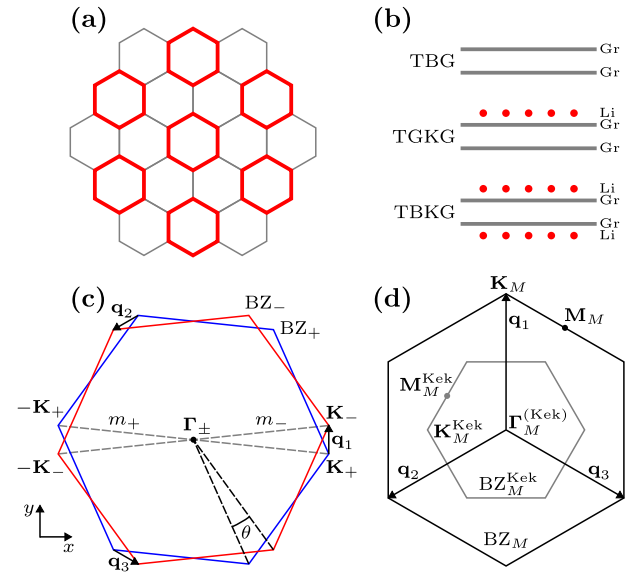


FIG. 1. (a) Kekulé-O bond order in graphene. The red and gray bonds indicate hoppings of different magnitudes between neighboring on-site carbon p_z orbitals. (b) TBG (top) and possible realizations of TGKG (middle) and TBKG (bottom) using intercalated or dilutely deposited lithium atoms (red) and graphene monolayers (gray). (c) The top ($l = +$) and bottom ($l = -$) layer graphene BZs before development of Kekulé-O order are labeled BZ_l . The Kekulé-O order induces Dirac masses m_l which couple the \mathbf{K}_l and $-\mathbf{K}_l$ points, as indicated. (d) The larger hexagon labeled BZ_M is the moiré BZ for TBG and TGKG. The smaller hexagon labeled BZ_M^{Kek} is the Kekulé moiré BZ for TBKG. The moiré \mathbf{q}_j vectors (defined in panel (c)) and high symmetry momenta in both BZs are shown.

TGKG is the same as that of TBG. For twist angle θ near 1° and Dirac mass $m \lesssim 200$ meV in one layer, TGKG exhibits an isolated two-orbital honeycomb lattice flat band model at charge neutrality. In particular, there is a magic angle $\theta \approx 0.7^\circ$ and Dirac mass $m \approx 100$ meV for which the second valence and conduction bands become extremely flat.

In the case of TBKG, the moiré unit cell is enlarged to a $\sqrt{3} \times \sqrt{3}$ supercell relative to TBG when both layers have nonzero Dirac mass. For twist angle θ near 1° and Dirac mass $m \gtrsim 100$ meV in both layers, the lowest valence and conduction bands in TBKG at charge neutrality are one-orbital kagome lattice flat bands, with bandwidths that generally decrease with increasing m and decreasing θ . The next two sets of connected valence and conduction bands in this regime are flat bands on triangular lattices.

Generic continuum model.— We consider a twisted bilayer moiré system in which each layer is either graphene or Kekulé-O graphene. We denote the top and bottom layers by $l = +$ and $l = -$, respectively. Layer l is rotated by angle $-l\theta/2$ relative to the aligned configuration, and the twist angle θ is small. We denote the lattice constant of layer l by a_l , and define the interlayer biaxial strain $\epsilon = \ln(a_-/a_+)$. The hexagonal Brillouin zone (BZ) of graphene layer l before the development of Kekulé-O order is shown in Fig. 1(c) and is denoted BZ $_l$.

The electrons at low energies in graphene layer l and valley $\eta = \pm$ without Kekulé-O order have a Dirac Hamil-

tonian $h_{l,\eta}(\mathbf{p}) = \hbar v_l(\eta\sigma_x p_x + \sigma_y p_y)$ at small momentum $\mathbf{p} = p_x \hat{\mathbf{x}} + p_y \hat{\mathbf{y}}$ measured from $\eta \mathbf{K}_l$, where the high symmetry momenta $\mathbf{K}_l = \frac{4\pi}{3a_l} R_{-l\theta/2} \hat{\mathbf{x}}$ are shown in Fig. 1(c). Here, v_l is the Fermi velocity of layer l , σ_0 is the 2×2 identity matrix, and σ_x , σ_y , and σ_z are the Pauli matrices. The Hamiltonian $h_{l,\eta}(\mathbf{p})$ is written in the graphene sublattice basis $\alpha = +$ and $\alpha = -$, which indicate sublattices A and B , respectively. We neglect spin degrees of freedom for simplicity.

A Kekulé-O order in layer l modifies the Fermi velocity v_l and induces an intervalley hopping term $m_l \sigma_x$ [33, 38] (see Supp. Sec. II). This intervalley term produces a Dirac electron energy gap of $2m_l$, and we refer to m_l as the Dirac mass. Additionally, we consider a potential energy difference E_Δ between the two layers, which can arise from chemical dopants or an out-of-plane displacement field.

In the continuum (i.e., small $|\mathbf{p}|$) limit, we denote the real space basis for Dirac electrons at position \mathbf{r} in layer l , valley η , and sublattice α by $|\mathbf{r}, l, \eta, \alpha\rangle$. The continuum Hamiltonian of this moiré system then takes the form $H = \int d^2\mathbf{r} |\mathbf{r}\rangle \mathcal{H}(\mathbf{r}) \langle \mathbf{r}|$, where

$$\mathcal{H}(\mathbf{r}) = \begin{pmatrix} E_\Delta \sigma_0 - i\hbar v_+ \boldsymbol{\sigma} \cdot \nabla & m_+ \sigma_x & T(\mathbf{r}) & 0 \\ m_+ \sigma_x & E_\Delta \sigma_0 + i\hbar v_+ \boldsymbol{\sigma}^* \cdot \nabla & 0 & T^*(\mathbf{r}) \\ T^\dagger(\mathbf{r}) & 0 & -i\hbar v_- \boldsymbol{\sigma} \cdot \nabla & m_- \sigma_x \\ 0 & T^T(\mathbf{r}) & m_- \sigma_x & i\hbar v_- \boldsymbol{\sigma}^* \cdot \nabla \end{pmatrix}, \quad (1)$$

we have defined the basis row vector

$$|\mathbf{r}\rangle = (|\mathbf{r}, +, +, +\rangle \quad |\mathbf{r}, +, +, -\rangle \quad |\mathbf{r}, +, -, +\rangle \quad |\mathbf{r}, +, -, -\rangle \quad |\mathbf{r}, -, +, +\rangle \quad |\mathbf{r}, -, +, -\rangle \quad |\mathbf{r}, -, -, +\rangle \quad |\mathbf{r}, -, -, -\rangle), \quad (2)$$

and $\boldsymbol{\sigma} = \sigma_x \hat{\mathbf{x}} + \sigma_y \hat{\mathbf{y}}$ is the Pauli matrix vector. The interlayer moiré potential takes the same form as that in TBG [1, 5], namely

$$T(\mathbf{r}) = \sum_{j=1}^3 T_{\mathbf{q}_j} e^{i\mathbf{q}_j \cdot \mathbf{r}}, \quad \mathbf{q}_j = R_{\zeta_j}(\mathbf{K}_- - \mathbf{K}_+), \quad (3)$$

$$T_{\mathbf{q}_j} = w_0 \sigma_0 + w_1 (\sigma_x \cos \zeta_j + \sigma_y \sin \zeta_j).$$

Here, $\zeta_j = \frac{2\pi}{3}(j-1)$, R_ζ is the rotation matrix of angle ζ , and w_0 and w_1 are the interlayer hoppings at AA and AB stacking positions, respectively. The \mathbf{q}_j vectors are illustrated in Fig. 1(c). We have neglected the $-l\theta/2$ rotations of the Dirac Hamiltonians in Eq. (1), which is a valid approximation for small θ [1, 5]. When $E_\Delta = 0$ and $a_+ = a_-$, H has a particle-hole symmetry $\mathcal{P}H\mathcal{P}^{-1} = -H$, where \mathcal{P} is given by

$$\mathcal{P} |\mathbf{r}, l, \eta, \alpha\rangle = \eta l |\mathcal{R}_{\hat{\mathbf{x}}} \mathbf{r}, l, \eta, -\alpha\rangle, \quad (4)$$

and where $\mathcal{R}_{\hat{\mathbf{x}}}$ is the reflection matrix for the yz plane. As discussed in Supp. Sec. I, this is different from but related to the particle-hole transformation previously discussed for TBG [4, 5]. Note that when $m_+ = m_- = E_\Delta = 0$,

$v_+ = v_-$, and $a_+ = a_-$, Eq. (1) reduces to the two-valley model for TBG.

To a good approximation, one can neglect any changes of parameters in Kekulé-O graphene compared to normal graphene except for the Dirac mass m_l . We take $a_\pm = a_{\text{Gr}} = 0.246$ nm and $v_\pm = v_{\text{Gr}}$ where $\hbar v_{\text{Gr}}/a_{\text{Gr}} = 2.5$ eV, so that the interlayer biaxial strain $\epsilon = 0$. We use $w_1 = 110$ meV and $w_0/w_1 = 0.8$, which are typical parameters for TBG near $\theta = 1^\circ$ [1, 39]. Additionally, we take $E_\Delta = 0$ for simplicity. Results with different parameter choices including various values of w_0/w_1 and nonzero values of E_Δ and ϵ are given in Supp. Sec. IV. Note that the sign of each Dirac mass m_l in Eq. (1) can be flipped by applying a unitary change of basis. As a result, we take $m_l \geq 0$ without loss of generality.

TGKG.— We first consider the TGKG system illustrated in Fig. 1(b), in which the top layer is Kekulé-O graphene with $m_+ \geq 0$ and the bottom layer is normal graphene with $m_- = 0$. In this case, the Hamiltonian commutes with the translation operators

$$T_{\mathbf{R}} |\mathbf{r}, l, \eta, \alpha\rangle = e^{i(\mathbf{q}_1 \cdot \mathbf{R})\eta(l-1)/2} |\mathbf{r} + \mathbf{R}, l, \eta, \alpha\rangle \quad (5)$$

for \mathbf{R} in the moiré superlattice L_M , which is defined as

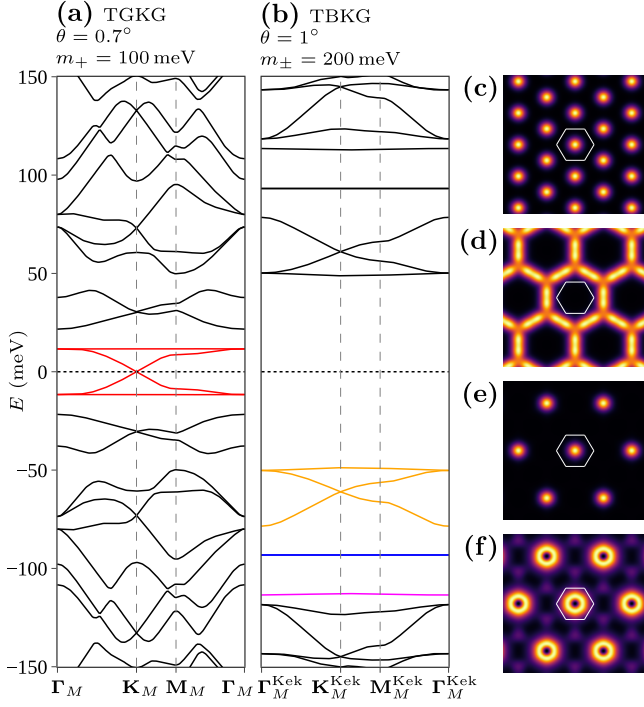


FIG. 2. (a) Band structure of TGKG with the magic parameters $\theta = 0.7^\circ$ and $m_+ = 100$ meV. Bands $-2 \leq n \leq 2$ (shown in red) have the symmetries of a two-orbital honeycomb lattice model. (b) Band structure of TBKG with $\theta = 1^\circ$ and $m_\pm = 200$ meV. Bands $-3 \leq n \leq -1$ (shown in orange), $-5 \leq n \leq -4$ (shown in blue), and $n = -6$ (shown in magenta) have the symmetries of one-orbital kagome lattice, two-orbital triangular lattice, and one-orbital triangular lattice models, respectively. The dashed black lines indicate the Fermi level at charge neutrality, which must be 0 because of the particle-hole symmetry in Eq. (4). (c)-(f) The total charge density of the bands shown in red (in panel (a)), orange, blue, and magenta (in panel (b)), respectively. In each plot, the white hexagon is a unit cell for the moiré superlattice L_M of TGKG. Note that (d)-(f) which are plots for TBKG show periodicity with respect to a $\sqrt{3} \times \sqrt{3}$ enlarged superlattice.

the reciprocal of the Bravais lattice P_M generated by $\mathbf{q}_1 - \mathbf{q}_2$ and $\mathbf{q}_1 - \mathbf{q}_3$. As a result, TGKG has the same moiré unit cell as TBG. The moiré BZ of TGKG is the larger hexagon BZ_M in Fig. 1(d).

TGKG generally has magnetic space group $P61'$ (#168.110 in the BNS setting [40]) generated by $T_{\mathbf{R}}$ for $\mathbf{R} \in L_M$, C_{6z} (rotation by $\pi/3$ about $\hat{\mathbf{z}}$), and \mathcal{T} (antiunitary spinless time-reversal). These operators are given in Supp. Tab. S1.

Fig. 2(a) shows the band structure of TGKG with $\theta = 0.7^\circ$ and $m_+ = 100$ meV. We use band index $n \neq 0$ to denote the $|n|$ -th conduction (valence) band for $n > 0$ ($n < 0$). The four connected bands $-2 \leq n \leq 2$ around charge neutrality (shown in red) are isolated from higher bands, and the two bands $n = \pm 2$ are extremely flat. Using magnetic topological quantum chemistry (MTQC) [41–43], we find that these four bands are consistent with

elementary band corepresentation (EBCR) $(^1E^2E)_{2b}$ of $P61'$. A full table of EBCRs for each magnetic space group can be found on the Bilbao Crystallographic Server [17, 43]. EBCR $(^1E^2E)_{2b}$ corresponds to a system with two orbitals per site on a honeycomb lattice L_{hc} . These four bands can be approximately described by the honeycomb lattice tight-binding model

$$H_{hc} = \sum_{\ell, \ell' = \pm 1} t_{\ell, \ell'} \sum_{\langle j, j' \rangle \in L_{hc}} e^{i(\ell - \ell')\varphi_{j', j}} |j', \ell'\rangle \langle j, \ell|. \quad (6)$$

Here, t_+ and t_- are real hopping parameters, $|j, \ell\rangle$ is an orbital with angular momentum ℓ modulo 3 on site j , $\langle j, j' \rangle$ runs over all nearest neighbors in L_{hc} , and $\varphi_{j', j}$ is the angle from an arbitrary fixed axis to the ray from site j to site j' . When $|t_+| = |t_-|$, the highest and lowest bands of this model are exactly flat [24, 25, 28]. See Supp. Sec. III for a construction of the compact localized states and noncontractible loop states for the flat bands in this case [44].

Although the Wannier orbitals for bands $-2 \leq n \leq 2$ must form a honeycomb lattice, their total charge density, shown in Fig. 2(c), is peaked on the triangular lattice formed by the AA stacking positions. A similar phenomenon occurs in magic angle TBG, in which case it is known that each Wannier orbital has a three-lobed “figet spinner” shape [45–47].

Fig. 3(a) shows the bandwidth of the $n = \pm 2$ two-orbital honeycomb lattice flat bands as a function of θ and m_+ . We observe two stripes in the parameter space in which the bandwidth reduces to approximately 1 meV. In particular, bandwidth minima are achieved in two regimes: near $\theta = 1^\circ$, $m_+ = 0$, which is the magic angle TBG regime, and near $\theta = 0.7^\circ$, $m_+ = 100$ meV, which we call the magic TGKG regime and illustrate in Fig. 2(a). The experimentally measured Dirac masses are approximately 200 meV with lithium intercalation [32] and 100 meV with dilute lithium deposition [34]. Therefore, the magic TGKG regime for honeycomb lattice flat bands is experimentally realistic.

TBKG.— We now consider the TBKG system illustrated in Fig. 1(b), in which both layers are Kekulé-O graphene. For simplicity, we assume equal Dirac masses $m_+ = m_- \geq 0$. When both m_\pm are nonzero, the Hamiltonian only commutes with the translation operators $T_{\mathbf{R}}$ in Eq. (5) for \mathbf{R} in the Kekulé moiré superlattice L_M^{Kek} , which is defined as the reciprocal of the Bravais lattice P_M^{Kek} generated by \mathbf{q}_1 and \mathbf{q}_2 . L_M^{Kek} is a $\sqrt{3} \times \sqrt{3}$ superlattice of L_M and the Kekulé moiré BZ is the smaller hexagon BZ_M^{Kek} in Fig. 1(d).

TBKG generally has magnetic space group $P61'$ just like TGKG. In the special case considered here in which $m_+ = m_-$ and $E_\Delta = 0$, the magnetic space group expands to $P6221'$ (#177.150 in the BNS setting [40]) because of the C_{2x} (rotation by π about the $\hat{\mathbf{x}}$) symmetry generator. However, we will use $P61'$ to emphasize that our results are stable against small C_{2x} symmetry breaking perturbations. The $P61'$ symmetry operators are given in Supp. Tab. S1.

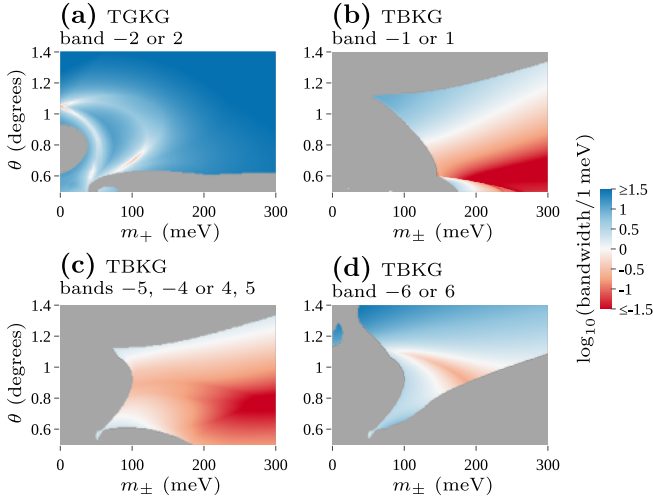


FIG. 3. (a) The bandwidth of band $n = \pm 2$ for TGKG as a function of θ and m_+ . (b)-(d) The bandwidth of band $n = \pm 1$, bands $-5 \leq n \leq -4$ or $4 \leq n \leq 5$, and band $n = \pm 6$ for TBKG, respectively, as a function of θ and m_+ . In (a)-(d) the non-gray regions show parameters for which MTQC analysis indicates EBCR (${}^1E^2E$)_{2b}, (B)_{3c}, (${}^1E^2E_2$)_{1a}, and (A)_{1a} of P61' for TGKG bands $-2 \leq n \leq 2$, TBKG bands $-3 \leq n \leq -1$, TBKG bands $-5 \leq n \leq -4$, and TBKG band $n = -6$, respectively.

Fig. 2(b) shows the band structure of TBKG with $\theta = 1^\circ$ and $m_\pm = 200$ meV. There are twelve low energy bands, which result from folding the four low energy bands of TBG into BZ_M^{Kek} and then adding the Dirac masses m_\pm . The six valence bands form three groups of connected bands. Using MTQC, we identify bands $-3 \leq n \leq -1$ (shown in orange), $-5 \leq n \leq -4$ (shown in blue), and $n = -6$ (shown in magenta) with EBCRs (B)_{3c}, (${}^1E^2E_2$)_{1a}, and (A)_{1a} of P61', respectively. The conduction bands are related to the valence bands by the particle-hole transformation \mathcal{P} in Eq. (4) and their EBCRs are given in Supp. Tab. S1. It is evident that bands $n = \pm 1, \pm 4, \pm 5, \pm 6$ are extremely flat.

We now consider the three groups of valence bands separately. First, EBCR (B)_{3c} corresponds to a system with a single orbital per site on a kagome lattice L_{kag} . Accordingly, bands $-3 \leq n \leq -1$ can be approximately described by the kagome lattice tight-binding model

$$H_{\text{kag}} = t \sum_{\langle j, j' \rangle \in L_{\text{kag}}} |j'\rangle \langle j|, \quad (7)$$

where t is a real hopping parameter, $|j\rangle$ is the orbital on site j , and $\langle j, j' \rangle$ runs over all nearest neighbors in L_{kag} . This Hamiltonian always has an exactly flat band [24, 26, 28] composed of compact localized states and noncontractible loop states [44], as explained in Supp. Sec. III. Fig. 2(d) shows the total charge density of bands $-3 \leq n \leq -1$, which is peaked at kagome lattice sites.

Next, EBCR (${}^1E^2E_2$)_{1a} corresponds to a system with two orbitals per site on a triangular lattice L_{tri} . Therefore, bands $-5 \leq n \leq -4$ can be approximately described

by the triangular lattice tight-binding model

$$H_{\text{tri-2}} = \sum_{\ell, \ell' = \pm 1} t_{\ell, \ell'} \sum_{\langle j, j' \rangle \in L_{\text{tri}}} e^{i(\ell - \ell')\varphi_{j', j}} |j', \ell'\rangle \langle j, \ell|. \quad (8)$$

The parameters and notations here are identical to those in Eq. (6) except that the sites j here form a triangular lattice. Fig. 2(e) shows the total charge density of bands $-5 \leq n \leq -4$, which is peaked at triangular lattice sites.

Finally, EBCR (A)_{1a} corresponds to a system with a single orbital per site on a triangular lattice L_{tri} . As a result, band $n = -6$ can be approximately described by the triangular lattice tight-binding model

$$H_{\text{tri-1}} = t \sum_{\langle j, j' \rangle \in L_{\text{tri}}} |j'\rangle \langle j|. \quad (9)$$

The parameters and notations here are identical to those in Eq. (7) except that the sites j here form a triangular lattice. Fig. 2(f) shows the total charge density of band $n = -6$, which has peaks surrounding triangular lattice sites.

Figs. 3(b)-(d) show the bandwidths of the $n = \pm 1$ one-orbital kagome lattice, $-5 \leq n \leq -4$ or $4 \leq n \leq 5$ two-orbital triangular lattice, and $n = \pm 6$ one-orbital triangular lattice flat bands, respectively, as a function of θ and m_\pm . The one-orbital kagome lattice and two-orbital triangular lattice bandwidths generally decrease with increasing m_\pm and decreasing θ . On the other hand, the one-orbital triangular lattice bandwidth is smallest for $0.8^\circ \lesssim \theta \lesssim 1.1^\circ$ and $100 \text{ meV} \lesssim m_\pm \lesssim 200 \text{ meV}$. The Dirac masses required to realize kagome lattice and triangular lattice flat bands in TBKG are thus experimentally realistic.

Discussion.— We have shown that for twist angles near $\theta = 1^\circ$ and Dirac masses m_l within an experimentally realistic range, TGKG exhibits a two-orbital honeycomb lattice flat band model at charge neutrality, while TBKG exhibits both kagome and triangular lattice flat band models at low energies which are quite robust against parameter variation. When interactions are included, the nontrivial flat bands of the honeycomb and kagome lattice models become promising highly tunable platforms for the realization of strongly correlated phases such as Mott insulators, charge or spin density waves, and spin liquids [48, 49]. We leave for future work the possibility of inducing spin-orbit coupling or magnetism through substrate coupling or other means. These effects generically produce flat (spin) Chern bands [28], in which fractional Chern or topological insulators may be realized [50].

For TGKG, when the Dirac mass is large ($m_+ \gtrsim 500$ meV), the Kekulé-O graphene layer has a sufficiently large gap to allow a perturbative treatment. As explained in [28], an effective moiré model can be derived for the non-Kekulé layer, in which the two valleys are coupled by a moiré potential. However, this perturbative model gives qualitatively incorrect band structures for small Dirac masses m_+ , and in such cases the full model in Eq. (1) is required.

In an ideal realization of TGKG or TBKG, care must be taken to avoid charge transfer from the adatoms inducing Kekulé-O order into the graphene layers, since the flat bands are near the charge neutrality point of pristine graphene. In Ref. [34] the authors used a dilute concentration of lithium adatoms with negligible charge transfer to the graphene layer, and observed a well-resolved Kekulé-O order despite the disordered adatom arrangement [33]. Charge transfer may also be avoided through intercalation or deposition of both donor and acceptor atoms, for instance, hydrogen and lithium atoms which hole-dope and electron-dope graphene, respectively [32, 34]. First principles calculations and ex-

perimental studies are needed to address these issues.

Acknowledgements.— We thank Ali Yazdani, Christopher Gutiérrez, Changhua Bao, Jonah Herzog-Arbeitman, and Yves H. Kwan for valuable discussions. This work is supported by the Alfred P. Sloan Foundation, the National Science Foundation through Princeton University’s Materials Research Science and Engineering Center DMR-2011750, and the National Science Foundation under award DMR-2141966. Additional support is provided by the Gordon and Betty Moore Foundation through Grant GBMF8685 towards the Princeton theory program.

-
- [1] R. Bistritzer and A. H. MacDonald, Moiré bands in twisted double-layer graphene, *Proceedings of the National Academy of Sciences of the United States of America* **108**, 12233 (2011), [arXiv:1009.4203](#).
 - [2] H. C. Po, L. Zou, T. Senthil, and A. Vishwanath, Faithful tight-binding models and fragile topology of magic-angle bilayer graphene, *Physical Review B* **99**, 1 (2019), [arXiv:1808.02482](#).
 - [3] J. Ahn, S. Park, and B. J. Yang, Failure of Nielsen-Ninomiya Theorem and Fragile Topology in Two-Dimensional Systems with Space-Time Inversion Symmetry: Application to Twisted Bilayer Graphene at Magic Angle, *Physical Review X* **9**, 21013 (2019), [arXiv:1808.05375](#).
 - [4] Z. Song, Z. Wang, W. Shi, G. Li, C. Fang, and B. A. Bernevig, All Magic Angles in Twisted Bilayer Graphene are Topological, *Physical Review Letters* **123**, 036401 (2019), [arXiv:1807.10676](#).
 - [5] Z.-D. Song, B. Lian, N. Regnault, and B. A. Bernevig, Twisted bilayer graphene. II. Stable symmetry anomaly, *Physical Review B* **103**, 205412 (2021).
 - [6] Y. Cao, V. Fatemi, S. Fang, K. Watanabe, T. Taniguchi, E. Kaxiras, and P. Jarillo-Herrero, Unconventional superconductivity in magic-angle graphene superlattices, *Nature* **556**, 43 (2018).
 - [7] Y. Cao, V. Fatemi, A. Demir, S. Fang, S. L. Tomarken, J. Y. Luo, J. D. Sanchez-Yamagishi, K. Watanabe, T. Taniguchi, E. Kaxiras, R. C. Ashoori, and P. Jarillo-Herrero, Correlated insulator behaviour at half-filling in magic-angle graphene superlattices, *Nature* **556**, 80 (2018).
 - [8] M. Yankowitz, S. Chen, H. Polshyn, Y. Zhang, K. Watanabe, T. Taniguchi, D. Graf, A. F. Young, and C. R. Dean, Tuning superconductivity in twisted bilayer graphene, *Science* **363**, 1059 (2019), [arXiv:1808.07865](#).
 - [9] A. L. Sharpe, E. J. Fox, A. W. Barnard, J. Finney, K. Watanabe, T. Taniguchi, M. A. Kastner, and D. Goldhaber-Gordon, Emergent ferromagnetism near three-quarters filling in twisted bilayer graphene, *Science* **365**, 605 (2019), [arXiv:1901.03520](#).
 - [10] X. Lu, P. Stepanov, W. Yang, M. Xie, M. A. Aamir, I. Das, C. Urgell, K. Watanabe, T. Taniguchi, G. Zhang, A. Bachtold, A. H. MacDonald, and D. K. Efetov, Superconductors, orbital magnets and correlated states in magic-angle bilayer graphene, *Nature* **574**, 653 (2019), [arXiv:1903.06513](#).
 - [11] M. Serlin, C. L. Tschirhart, H. Polshyn, Y. Zhang, J. Zhu, K. Watanabe, T. Taniguchi, L. Balents, and A. F. Young, Intrinsic quantized anomalous Hall effect in a moiré heterostructure, *Science* **367**, 900 (2020), [arXiv:1907.00261](#).
 - [12] K. P. Nuckolls, M. Oh, D. Wong, B. Lian, K. Watanabe, T. Taniguchi, B. A. Bernevig, and A. Yazdani, Strongly correlated Chern insulators in magic-angle twisted bilayer graphene, *Nature* **588**, 610 (2020), [arXiv:2007.03810](#).
 - [13] Y. Xie, A. T. Pierce, J. M. Park, D. E. Parker, E. Khalaf, P. Ledwith, Y. Cao, S. H. Lee, S. Chen, P. R. Forrester, K. Watanabe, T. Taniguchi, A. Vishwanath, P. Jarillo-Herrero, and A. Yacoby, Fractional Chern insulators in magic-angle twisted bilayer graphene, *Nature* **600**, 439 (2021), [arXiv:2107.10854](#).
 - [14] G. Chen, A. L. Sharpe, P. Gallagher, I. T. Rosen, E. J. Fox, L. Jiang, B. Lyu, H. Li, K. Watanabe, T. Taniguchi, J. Jung, Z. Shi, D. Goldhaber-Gordon, Y. Zhang, and F. Wang, Signatures of tunable superconductivity in a trilayer graphene moiré superlattice, *Nature* **572**, 215 (2019).
 - [15] J. M. Park, Y. Cao, K. Watanabe, T. Taniguchi, and P. Jarillo-Herrero, Tunable strongly coupled superconductivity in magic-angle twisted trilayer graphene, *Nature* **590**, 249 (2021).
 - [16] Z. Hao, A. M. Zimmerman, P. Ledwith, E. Khalaf, D. H. Najafabadi, K. Watanabe, T. Taniguchi, A. Vishwanath, and P. Kim, Electric field-tunable superconductivity in alternating-twist magic-angle trilayer graphene, *Science* **371**, 1133 (2021).
 - [17] Y. Xu, S. Liu, D. A. Rhodes, K. Watanabe, T. Taniguchi, J. Hone, V. Elser, K. F. Mak, and J. Shan, Correlated insulating states at fractional fillings of moiré superlattices, *Nature* **587**, 214 (2020).
 - [18] Z. Zhang, Y. Wang, K. Watanabe, T. Taniguchi, K. Ueno, E. Tutuc, and B. J. LeRoy, Flat bands in twisted bilayer transition metal dichalcogenides, *Nature Physics* **16**, 1093 (2020).
 - [19] B. A. Foutty, C. R. Kometter, T. Devakul, A. P. Reddy, K. Watanabe, T. Taniguchi, L. Fu, and B. E. Feldman, Mapping twist-tuned multi-band topology in bilayer WSe₂, **2** (2023), [arXiv:2304.09808](#).
 - [20] J. Cai, E. Anderson, C. Wang, X. Zhang, X. Liu, W. Holtzmann, Y. Zhang, F. Fan, T. Taniguchi,

- K. Watanabe, Y. Ran, T. Cao, L. Fu, D. Xiao, W. Yao, and X. Xu, Signatures of Fractional Quantum Anomalous Hall States in Twisted MoTe₂ Bilayer, (2023), [arXiv:2304.08470](#).
- [21] Y. Zeng, Z. Xia, K. Kang, J. Zhu, P. Knüppel, C. Vaswani, K. Watanabe, T. Taniguchi, K. F. Mak, and J. Shan, Integer and fractional Chern insulators in twisted bilayer MoTe₂, , 29 (2023), [arXiv:2305.00973](#).
- [22] E. H. Lieb, Two theorems on the Hubbard model, *Physical Review Letters* **62**, 1201 (1989).
- [23] A. Mielke, Ferromagnetic ground states for the Hubbard model on line graphs, *Journal of Physics A: Mathematical and General* **24**, L73 (1991).
- [24] D. Călugăru, A. Chew, L. Elcoro, Y. Xu, N. Regnault, Z. D. Song, and B. A. Bernevig, General construction and topological classification of crystalline flat bands, *Nature Physics* **18**, 185 (2022).
- [25] C. Wu, D. Bergman, L. Balents, and S. Das Sarma, Flat bands and wigner crystallization in the honeycomb optical lattice, *Physical Review Letters* **99**, 1 (2007), [arXiv:0701788 \[cond-mat\]](#).
- [26] D. L. Bergman, C. Wu, and L. Balents, Band touching from real-space topology in frustrated hopping models, *Physical Review B - Condensed Matter and Materials Physics* **78**, 1 (2008), [arXiv:0803.3628](#).
- [27] M. G. Scheer, K. Gu, and B. Lian, Magic angles in twisted bilayer graphene near commensuration: Towards a hypermagic regime, *Physical Review B* **106**, 115418 (2022), [arXiv:2203.06163](#).
- [28] M. G. Scheer and B. Lian, Kagome and honeycomb flat bands in moiré graphene, *Physical Review B* **108**, 245136 (2023).
- [29] C. Gutiérrez, C. J. Kim, L. Brown, T. Schiros, D. Nordlund, E. B. Lochocki, K. M. Shen, J. Park, and A. N. Pasupathy, Imaging chiral symmetry breaking from Kekulé bond order in graphene, *Nature Physics* **12**, 950 (2016).
- [30] K. Sugawara, K. Kanetani, T. Sato, and T. Takahashi, Fabrication of Li-intercalated bilayer graphene, *AIP Advances* **1**, 10.1063/1.3582814 (2011).
- [31] K. Kanetani, K. Sugawara, T. Sato, R. Shimizu, K. Iwaya, T. Hitosugi, and T. Takahashi, Ca intercalated bilayer graphene as a thinnest limit of superconducting C₆Ca, *Proceedings of the National Academy of Sciences of the United States of America* **109**, 19610 (2012).
- [32] C. Bao, H. Zhang, T. Zhang, X. Wu, L. Luo, S. Zhou, Q. Li, Y. Hou, W. Yao, L. Liu, P. Yu, J. Li, W. Duan, H. Yao, Y. Wang, and S. Zhou, Experimental Evidence of Chiral Symmetry Breaking in Kekulé-Ordered Graphene, *Physical Review Letters* **126**, 1 (2021), [arXiv:2106.01359](#).
- [33] V. V. Cheianov, V. I. Fal'ko, O. Syljuåsen, and B. L. Altshuler, Hidden Kekulé ordering of adatoms on graphene, *Solid State Communications* **149**, 1499 (2009).
- [34] A. C. Qu, P. Nigge, S. Link, G. Levy, M. Michiardi, P. L. Spandar, T. Matthé, M. Schneider, S. Zhdanovich, U. Starke, C. Gutiérrez, and A. Damascelli, Ubiquitous defect-induced density wave instability in monolayer graphene, *Science Advances* **8**, 1 (2022).
- [35] S. Y. Li, Y. Zhang, L. J. Yin, and L. He, Scanning tunneling microscope study of quantum Hall isospin ferromagnetic states in the zero Landau level in a graphene monolayer, *Physical Review B* **100**, 1 (2019).
- [36] X. Liu, G. Farahi, C. L. Chiu, Z. Papic, K. Watanabe, T. Taniguchi, M. P. Zaletel, and A. Yazdani, Visualizing broken symmetry and topological defects in a quantum Hall ferromagnet, *Science* **375**, 321 (2022), [arXiv:2109.11555](#).
- [37] K. P. Nuckolls, R. L. Lee, M. Oh, D. Wong, T. Soejima, J. P. Hong, D. Călugăru, J. Herzog-Arbeitman, B. A. Bernevig, K. Watanabe, T. Taniguchi, N. Regnault, M. P. Zaletel, and A. Yazdani, Quantum textures of the many-body wavefunctions in magic-angle graphene, (2023), [arXiv:2303.00024](#).
- [38] O. V. Gamayun, V. P. Ostroukh, N. V. Gnezdilov, I. Adagideli, and C. W. Beenakker, Valley-momentum locking in a graphene superlattice with Y-shaped Kekulé bond texture, *New Journal of Physics* **20**, 10.1088/1367-2630/aaa7e5 (2018), [arXiv:1708.08348](#).
- [39] S. Carr, S. Fang, Z. Zhu, and E. Kaxiras, Exact continuum model for low-energy electronic states of twisted bilayer graphene, *Physical Review Research* **1**, 1 (2019), [arXiv:1901.03420](#).
- [40] S. V. Gallego, E. S. Tasci, G. de la Flor, J. M. Perez-Mato, and M. I. Aroyo, Magnetic symmetry in the Bilbao Crystallographic Server: a computer program to provide systematic absences of magnetic neutron diffraction, *Journal of Applied Crystallography* **45**, 1236 (2012).
- [41] B. Bradlyn, L. Elcoro, J. Cano, M. G. Vergniory, Z. Wang, C. Felser, M. I. Aroyo, and B. A. Bernevig, Topological quantum chemistry, *Nature* **547**, 298 (2017), [arXiv:1703.02050](#).
- [42] J. Kruthoff, J. De Boer, J. Van Wezel, C. L. Kane, and R. J. Slager, Topological classification of crystalline insulators through band structure combinatorics, *Physical Review X* **7**, 1 (2017), [arXiv:1612.02007](#).
- [43] L. Elcoro, B. J. Wieder, Z. Song, Y. Xu, B. Bradlyn, and B. A. Bernevig, Magnetic topological quantum chemistry, *Nature Communications* **12**, 4 (2021), [arXiv:2010.00598](#).
- [44] J. W. Rhim and B. J. Yang, Classification of flat bands according to the band-crossing singularity of Bloch wave functions, *Physical Review B* **99**, 1 (2019), [arXiv:1808.05926](#).
- [45] M. Koshino, N. F. Yuan, T. Koretsune, M. Ochi, K. Kuroki, and L. Fu, Maximally Localized Wannier Orbitals and the Extended Hubbard Model for Twisted Bilayer Graphene, *Physical Review X* **8**, 31087 (2018), [arXiv:1805.06819](#).
- [46] J. Kang and O. Vafek, Symmetry, Maximally Localized Wannier States, and a Low-Energy Model for Twisted Bilayer Graphene Narrow Bands, *Physical Review X* **8**, 31088 (2018), [arXiv:1805.04918](#).
- [47] H. C. Po, L. Zou, A. Vishwanath, and T. Senthil, Origin of Mott Insulating Behavior and Superconductivity in Twisted Bilayer Graphene, *Physical Review X* **8**, 31089 (2018), [arXiv:1803.09742](#).
- [48] S. Yan, D. A. Huse, and S. R. White, Spin-Liquid Ground State of the $S = 1/2$ Kagome Heisenberg Antiferromagnet, *Science* **332**, 1173 (2011).
- [49] J. X. Yin, B. Lian, and M. Z. Hasan, Topological kagome magnets and superconductors, *Nature* **612**, 647 (2022), [arXiv:2212.11628](#).
- [50] E. Tang, J. W. Mei, and X. G. Wen, High-temperature fractional quantum hall states, *Physical Review Letters* **106**, 10 (2011), [arXiv:1012.2930](#).
- [51] Y. Xu, L. Elcoro, Z. D. Song, B. J. Wieder, M. G. Vergniory, N. Regnault, Y. Chen, C. Felser, and B. A. Bernevig, High-throughput calculations of magnetic topological materials, *Nature* **586**, 702 (2020), [arXiv:2003.00012](#).

- [52] Z. Wang, S. M. Selbach, and T. Grande, Van der Waals density functional study of the energetics of alkali metal intercalation in graphite, *RSC Advances* **4**, 4069 (2014).

Supplemental Material

I. SYMMETRIES

We now consider the crystalline symmetries of the Hamiltonian H given in Eq. (1). The moiré and Kekulé moiré reciprocal lattices P_M and P_M^{Kek} are Bravais lattices given by

$$\begin{aligned} P_M &= \{n_1 \mathbf{q}_1 + n_2 \mathbf{q}_2 + n_3 \mathbf{q}_3 | n_1, n_2, n_3 \in \mathbb{Z}, n_1 + n_2 + n_3 = 0\}, \\ P_M^{\text{Kek}} &= \frac{1}{\sqrt{3}} R_{\pi/2} P_M = \{n_1 \mathbf{q}_1 + n_2 \mathbf{q}_2 + n_3 \mathbf{q}_3 | n_1, n_2, n_3 \in \mathbb{Z}\}. \end{aligned} \quad (\text{S1})$$

The moiré and Kekulé moiré superlattices L_M and $L_M^{\text{Kek}} = \sqrt{3} R_{\pi/2} L_M$ are reciprocal to P_M and P_M^{Kek} , respectively. H is always invariant under translation by elements of L_M^{Kek} . However, in TBG or TGKG there are also translation operators for elements in L_M that commute with H . For a vector \mathbf{R} , we write $T_{\mathbf{R}}$ for the translation by \mathbf{R} . The other relevant crystalline symmetry generators are C_{3z} (rotation by $2\pi/3$ about $\hat{\mathbf{z}}$), C_{2z} (rotation by π about $\hat{\mathbf{z}}$), C_{2x} (rotation by π about $\hat{\mathbf{x}}$), and \mathcal{T} (antiunitary spinless time-reversal). See Tab. S1 for an enumeration of the magnetic space group corepresentations that commute with H in several important cases. In each case, we give an example band corepresentation decomposition [41–43] for the low energy bands.

The Hamiltonian for TBG (i.e., Eq. (1) with $m_+ = m_- = E_{\Delta} = 0$, $v_+ = v_-$, and $a_+ = a_-$) anticommutes with a particle-hole symmetry operator [4, 5]

$$\mathcal{P}_0 |\mathbf{r}, l, \eta, \alpha\rangle = \eta l |-\mathbf{r}, -l, \eta, \alpha\rangle \quad (\text{S2})$$

and commutes with C_{2x} , which takes the form

$$C_{2x} |\mathbf{r}, l, \eta, \alpha\rangle = -|\mathcal{R}_{\hat{\mathbf{y}}} \mathbf{r}, -l, \eta, -\alpha\rangle. \quad (\text{S3})$$

Here, $\mathcal{R}_{\hat{\mathbf{y}}}$ is the reflection matrix for the xz plane. Both of these symmetries are broken when $m_+ \neq m_-$, $E_{\Delta} \neq 0$, $v_+ \neq v_-$, or $a_+ \neq a_-$ in Eq. (1). However, as long as $E_{\Delta} = 0$ and $a_+ = a_-$, the Hamiltonian in Eq. (1) anticommutes with the combined particle-hole symmetry operator $\mathcal{P} = -C_{2x} \mathcal{P}_0$, which takes the form

$$\mathcal{P} |\mathbf{r}, l, \eta, \alpha\rangle = \eta l |\mathcal{R}_{\hat{\mathbf{x}}} \mathbf{r}, l, \eta, -\alpha\rangle. \quad (\text{S4})$$

Here, $\mathcal{R}_{\hat{\mathbf{x}}}$ is the reflection matrix for the yz plane.

II. KEKULÉ-O GRAPHENE

In the following subsections, we derive and analyze tight-binding models and low energy continuum models for graphene both with and without a Kekulé-O distortion. As illustrated in Fig. S1(a), we consider a nearest neighbor tight-binding model with a single p_z orbital on each site of a honeycomb lattice. For simplicity, we neglect spin degrees of freedom. The nearest neighbor bonds shown with thick red lines (thin gray lines) have real hopping parameter $-t$ ($-s$).

We denote by L the triangular Bravais lattice formed by the centers of all the hexagons. Similarly, we define $L^{\text{Kek}} = \sqrt{3} R_{\pi/2} L$ to be the Bravais lattice formed by the centers of all the hexagons bounded by thick red lines. The primitive vectors \mathbf{a}_1 and \mathbf{a}_2 ($\mathbf{a}_1^{\text{Kek}}$ and $\mathbf{a}_2^{\text{Kek}}$) for L (L^{Kek}) are shown in Fig. S1(a). These primitive vectors are given by

$$\mathbf{a}_1 = a \hat{\mathbf{x}}, \quad \mathbf{a}_2 = R_{-\pi/3} \mathbf{a}_1, \quad \mathbf{a}_1^{\text{Kek}} = \sqrt{3} R_{\pi/2} \mathbf{a}_1, \quad \mathbf{a}_2^{\text{Kek}} = \sqrt{3} R_{\pi/2} \mathbf{a}_2 \quad (\text{S5})$$

for a positive constant a .

We denote the lattices reciprocal to L and L^{Kek} by P and $P^{\text{Kek}} = R_{\pi/2} P / \sqrt{3}$, respectively. The primitive vectors \mathbf{b}_1 and \mathbf{b}_2 ($\mathbf{b}_1^{\text{Kek}}$ and $\mathbf{b}_2^{\text{Kek}}$) for P (P^{Kek}) are given by

$$\mathbf{b}_1 = R_{2\pi/3} \mathbf{b}_2, \quad \mathbf{b}_2 = -4\pi \hat{\mathbf{y}} / (a\sqrt{3}), \quad \mathbf{b}_1^{\text{Kek}} = R_{\pi/2} \mathbf{b}_1 / \sqrt{3}, \quad \mathbf{b}_2^{\text{Kek}} = R_{\pi/2} \mathbf{b}_2 / \sqrt{3}. \quad (\text{S6})$$

We define high symmetry crystal momenta

$$\mathbf{\Gamma} = \mathbf{0}, \quad \mathbf{K} = \frac{2}{3} \mathbf{b}_1 + \frac{1}{3} \mathbf{b}_2, \quad \mathbf{M} = \frac{1}{2} \mathbf{b}_1 + \frac{1}{2} \mathbf{b}_2, \quad \mathbf{\Gamma}^{\text{Kek}} = \mathbf{0}, \quad \mathbf{K}^{\text{Kek}} = R_{\pi/2} \mathbf{K} / \sqrt{3}, \quad \mathbf{M}^{\text{Kek}} = R_{\pi/2} \mathbf{M} / \sqrt{3}. \quad (\text{S7})$$

#	System	Constraints	Magnetic space group	Bravais lattice	Corep generators	Example band corep decomp
1	TBG	Valley η only $m_+ = m_- = 0$ $v_+ = v_-$ $E_\Delta = 0$	$P6'2'2$ (#177.151)	L_M	$T_{\mathbf{R}} \mathbf{r}\rangle_\eta = \mathbf{r} + \mathbf{R}\rangle_\eta e^{-i\eta(\mathbf{q}_1 \cdot \mathbf{R})\sigma_z} \otimes \sigma_0$ $C_{3z} \mathbf{r}\rangle_\eta = R_{2\pi/3}\mathbf{r}\rangle_\eta \sigma_0 \otimes e^{i\eta(2\pi/3)\sigma_z}$ $C_{2x} \mathbf{r}\rangle = - \mathcal{R}_{\hat{y}}\mathbf{r}\rangle \sigma_x \otimes \sigma_x$ $C_{2z}\mathcal{T} \mathbf{r}\rangle_\eta = -\mathbf{r}\rangle_\eta \sigma_0 \otimes \sigma_x$	$-1 \leq n \leq 1:$ $(A_1)_{2c} \oplus (A_2)_{1a} \oplus (A_1)_{1a}$
2	TBG	$m_+ = m_- = 0$ $v_+ = v_-$ $E_\Delta = 0$	$P6221'$ (#177.150)	L_M	$T_{\mathbf{R}} \mathbf{r}\rangle = \mathbf{r} + \mathbf{R}\rangle e^{-i(\mathbf{q}_1 \cdot \mathbf{R})\sigma_z \otimes \sigma_z} \otimes \sigma_0$ $C_{3z} \mathbf{r}\rangle = R_{2\pi/3}\mathbf{r}\rangle \sigma_0 \otimes e^{i(2\pi/3)\sigma_z \otimes \sigma_z}$ $C_{2z} \mathbf{r}\rangle = -\mathbf{r}\rangle \sigma_0 \otimes \sigma_x \otimes \sigma_x$ $C_{2x} \mathbf{r}\rangle = - \mathcal{R}_{\hat{y}}\mathbf{r}\rangle \sigma_x \otimes \sigma_0 \otimes \sigma_x$ $\mathcal{T} \mathbf{r}\rangle = \mathbf{r}\rangle \sigma_0 \otimes \sigma_x \otimes \sigma_0$	$-2 \leq n \leq 2:$ $(A_2)_{2c} \oplus (A_1)_{2c}$
3	TGKG	$m_- = 0$	$P61'$ (#168.110)	L_M	$T_{\mathbf{R}} \mathbf{r}\rangle = \mathbf{r} + \mathbf{R}\rangle (\sigma_0 \otimes \sigma_0) \oplus (e^{-i(\mathbf{q}_1 \cdot \mathbf{R})\sigma_z} \otimes \sigma_0)$ $C_{3z} \mathbf{r}\rangle = R_{2\pi/3}\mathbf{r}\rangle \sigma_0 \otimes e^{i(2\pi/3)\sigma_z \otimes \sigma_z}$ $C_{2z} \mathbf{r}\rangle = -\mathbf{r}\rangle \sigma_0 \otimes \sigma_x \otimes \sigma_x$ $\mathcal{T} \mathbf{r}\rangle = \mathbf{r}\rangle \sigma_0 \otimes \sigma_x \otimes \sigma_0$	$-2 \leq n \leq 2:$ $(^1E^2E)_{2b}$
4	TGKG	$m_+ = 0$	$P61'$ (#168.110)	L_M	$T_{\mathbf{R}} \mathbf{r}\rangle = \mathbf{r} + \mathbf{R}\rangle (e^{i(\mathbf{q}_1 \cdot \mathbf{R})\sigma_z} \otimes \sigma_0) \oplus (\sigma_0 \otimes \sigma_0)$ $C_{3z} \mathbf{r}\rangle = R_{2\pi/3}\mathbf{r}\rangle \sigma_0 \otimes e^{i(2\pi/3)\sigma_z \otimes \sigma_z}$ $C_{2z} \mathbf{r}\rangle = -\mathbf{r}\rangle \sigma_0 \otimes \sigma_x \otimes \sigma_x$ $\mathcal{T} \mathbf{r}\rangle = \mathbf{r}\rangle \sigma_0 \otimes \sigma_x \otimes \sigma_0$	$-2 \leq n \leq 2:$ $(^1E^2E)_{2b}$
5	TBKG	N/A	$P61'$ (#168.110)	L_M^{Kek}	$T_{\mathbf{R}} \mathbf{r}\rangle = \mathbf{r} + \mathbf{R}\rangle$ $C_{3z} \mathbf{r}\rangle = R_{2\pi/3}\mathbf{r}\rangle \sigma_0 \otimes e^{i(2\pi/3)\sigma_z \otimes \sigma_z}$ $C_{2z} \mathbf{r}\rangle = -\mathbf{r}\rangle \sigma_0 \otimes \sigma_x \otimes \sigma_x$ $\mathcal{T} \mathbf{r}\rangle = \mathbf{r}\rangle \sigma_0 \otimes \sigma_x \otimes \sigma_0$	$n = 6: (B)_{1a}$ $4 \leq n \leq 5: (^1E_1^2E_1)_{1a}$ $1 \leq n \leq 3: (A)_{3c}$ $-3 \leq n \leq -1: (B)_{3c}$ $-5 \leq n \leq -4: (^1E_2^2E_2)_{1a}$ $n = -6: (A)_{1a}$

TABLE S1. Magnetic topological quantum chemistry [41–43] analysis for the model in Eq. (1) in several cases. Row 1 describes a one-valley model while rows 2 through 5 describe two-valley models. The basis vector $|\mathbf{r}\rangle$ is defined in Eq. (2) so that the tensor product factors for all two-valley models are layer, valley, and sublattice, in that order. For the one-valley model, we use $|\mathbf{r}\rangle_\eta = (|\mathbf{r}, +, \eta, +\rangle \quad |\mathbf{r}, +, \eta, -\rangle \quad |\mathbf{r}, -, \eta, +\rangle \quad |\mathbf{r}, -, \eta, -\rangle)$ so that the tensor product factors are layer and sublattice, in that order. $R_{2\pi/3}$ is the rotation matrix of angle $2\pi/3$ and $R_{\hat{y}}$ is the reflection matrix for xz plane. The numbers for the magnetic space groups are given in the BNS setting [40] and elementary band corepresentation tables for each magnetic space group can be found on the Bilbao Crystallographic Server [43, 51]. For each band corepresentation decomposition, we use $w_1 = 110$ meV, $w_0/w_1 = 0.8$, $E_\Delta = 0$, $a_\pm = a_{\text{Gr}} = 0.246$ nm, and $v_\pm = v_{\text{Gr}}$, where $\hbar v_{\text{Gr}}/a_{\text{Gr}} = 2.5$ eV. The other parameters are as follows. In rows 1 and 2, we use $\theta = 1^\circ$ and $m_\pm = 0$. In row 3, we use $\theta = 0.7^\circ$, $m_+ = 100$ meV, and $m_- = 0$, as in Fig. 2(a). In row 4, we use $\theta = 0.7^\circ$, $m_+ = 0$, and $m_- = 100$ meV. In row 5, we use $\theta = 1^\circ$, and $m_+ = m_- = 200$ meV, as in Fig. 2(b).

The Brillouin zones BZ and BZ^{Kek} and the high symmetry crystal momenta are illustrated in Fig. S1(b). Note that

$$\mathbf{K} = 4\pi\hat{\mathbf{x}}/(3a) = \mathbf{b}_2^{\text{Kek}} \quad (\text{S8})$$

so that $\mathbf{\Gamma}$, \mathbf{K} , and $-\mathbf{K}$ are all elements of P^{Kek} .

A. Without Kekulé-O distortion

We first consider the special case in which $s = t$ so that the model is symmetric under translation by elements of L and the system has lattice constant a . We enumerate the lattice sites as $\mathbf{r} + \alpha\boldsymbol{\tau}$ for $\mathbf{r} \in L$ and $\alpha \in \{+, -\}$, where

$$\boldsymbol{\tau} = R_{\pi/2}\mathbf{a}_1/\sqrt{3}. \quad (\text{S9})$$

The A and B sublattices correspond here to sites with $\alpha = +$ and $\alpha = -$, respectively. We denote the orbital at site $\mathbf{r} + \alpha\boldsymbol{\tau}$ by $|\mathbf{r}, \alpha\rangle$ and define Bloch states

$$|\mathbf{k}, \alpha\rangle = \frac{1}{\sqrt{|\text{BZ}|}} \sum_{\mathbf{r} \in L} e^{i\mathbf{k} \cdot (\mathbf{r} + \alpha\boldsymbol{\tau})} |\mathbf{r}, \alpha\rangle. \quad (\text{S10})$$

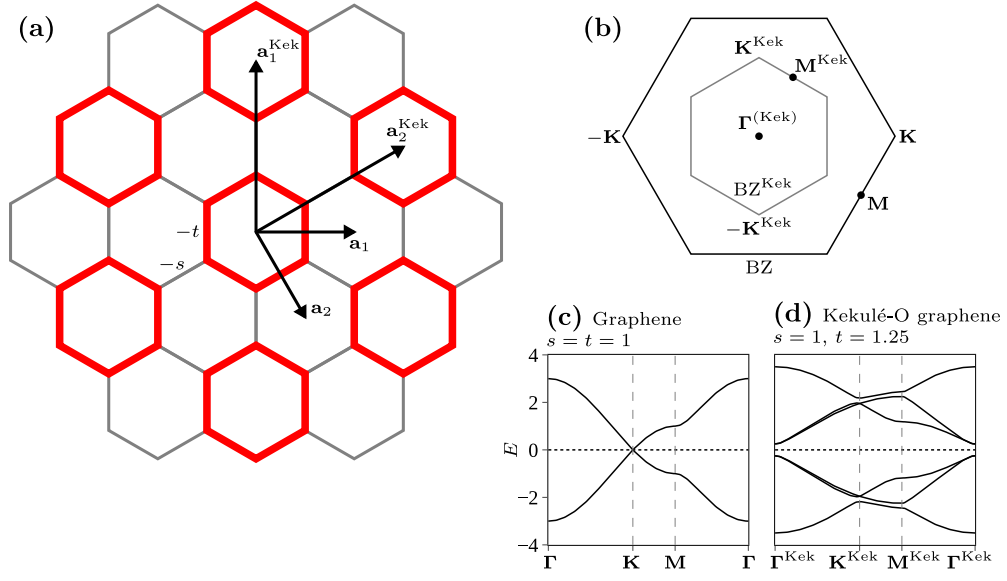


FIG. S1. (a) Illustration of the lattice vectors and hoppings for Kekulé-O bond order in graphene. (b) The graphene BZ (black), Kekulé BZ (gray), and their high symmetry momenta. (c) Example gapless band structure of graphene using the Hamiltonian in Eq. (S12) with $t = 1$. (d) Example band structure of Kekulé-O graphene using the Hamiltonian in Eq. (S21) with $s = 1, t = 1.25$. There is an energy gap of $2|t - s| = 0.5$.

These Bloch states carry a corepresentation of the magnetic space group $P6mm1'$ (#183.186 in the BNS setting [40]) determined by

$$\begin{aligned}
 T_{\mathbf{R}} |\mathbf{k}, \alpha\rangle &= e^{-i\mathbf{k} \cdot \mathbf{R}} |\mathbf{k}, \alpha\rangle, \\
 C_{3z} |\mathbf{k}, \alpha\rangle &= |R_{2\pi/3} \mathbf{k}, \alpha\rangle, \\
 M_x |\mathbf{k}, \alpha\rangle &= |\mathcal{R}_{\hat{x}} \mathbf{k}, \alpha\rangle, \\
 M_y |\mathbf{k}, \alpha\rangle &= |\mathcal{R}_{\hat{y}} \mathbf{k}, -\alpha\rangle, \\
 \mathcal{T} |\mathbf{k}, \alpha\rangle &= |-\mathbf{k}, \alpha\rangle,
 \end{aligned} \tag{S11}$$

where $T_{\mathbf{R}}$ denotes translation by $\mathbf{R} \in L$, C_{3z} denotes rotation by $2\pi/3$ about \hat{z} , M_x denotes reflection through the yz plane, M_y denotes reflection through the xz plane, and \mathcal{T} denotes antilinear spinless time-reversal. One could enlarge the group by considering also three dimensional inversion symmetry, but for simplicity we will not do so. The Hamiltonian commutes with the operators in Eq. (S11) and takes the form

$$H |\mathbf{k}, \alpha\rangle = -t \sum_{j=1}^3 e^{-i\alpha \mathbf{k} \cdot R_{\zeta_j} \boldsymbol{\tau}} |\mathbf{k}, -\alpha\rangle. \tag{S12}$$

Equivalently, for a fixed \mathbf{k} the Hamiltonian acts as the matrix

$$-t \sum_{j=1}^3 \begin{pmatrix} 0 & e^{i\mathbf{k} \cdot R_{\zeta_j} \boldsymbol{\tau}} \\ e^{-i\mathbf{k} \cdot R_{\zeta_j} \boldsymbol{\tau}} & 0 \end{pmatrix} \tag{S13}$$

in the basis $|\mathbf{k}, +\rangle, |\mathbf{k}, -\rangle$.

As shown in Fig. S1(c), the low energy physics for the Hamiltonian in Eq. (S12) consists of Dirac cones at the \mathbf{K} and $-\mathbf{K}$ points. To investigate this analytically, we take $\mathbf{k} = \eta \mathbf{K} + \mathbf{p}$ for $\eta \in \{+, -\}$ and expand $H |\mathbf{k}, \alpha\rangle$ to first order in $|\mathbf{p}|$. Using the identity

$$\mathbf{K} \cdot R_{\zeta_j} \boldsymbol{\tau} = -\zeta_j \tag{S14}$$

for $j \in \{1, 2, 3\}$, we have

$$\begin{aligned}
H |\eta \mathbf{K} + \mathbf{p}, \alpha\rangle &= -t \sum_{j=1}^3 e^{i\eta\alpha\zeta_j} e^{-i\alpha\mathbf{p} \cdot R_{\zeta_j} \boldsymbol{\tau}} |\eta \mathbf{K} + \mathbf{p}, -\alpha\rangle \\
&\approx -t \sum_{j=1}^3 e^{i\eta\alpha\zeta_j} (1 - i\alpha\mathbf{p} \cdot R_{\zeta_j} \boldsymbol{\tau}) |\eta \mathbf{K} + \mathbf{p}, -\alpha\rangle \\
&= \mathbf{p} \cdot \left(\frac{i\alpha at}{\sqrt{3}} \sum_{j=1}^3 e^{i\eta\alpha\zeta_j} R_{\zeta_j} \hat{\mathbf{y}} \right) |\eta \mathbf{K} + \mathbf{p}, -\alpha\rangle \\
&= \hbar v_F \mathbf{p} \cdot (\eta \hat{\mathbf{x}} + i\alpha \hat{\mathbf{y}}) |\eta \mathbf{K} + \mathbf{p}, -\alpha\rangle
\end{aligned} \tag{S15}$$

where

$$v_F = \frac{at\sqrt{3}}{2\hbar}. \tag{S16}$$

Equivalently, for a fixed η and \mathbf{p} the Hamiltonian acts as the matrix

$$\hbar v_F (\eta \sigma_x \hat{\mathbf{x}} + \sigma_y \hat{\mathbf{y}}) \cdot \mathbf{p} \tag{S17}$$

in the basis $|\eta \mathbf{K} + \mathbf{p}, +\rangle, |\eta \mathbf{K} + \mathbf{p}, -\rangle$, to first order in $|\mathbf{p}|$. We recognize Eq. (S17) as a Dirac cone with Fermi velocity v_F .

It will also be useful in the next section to expand $H |\boldsymbol{\Gamma} + \mathbf{p}, \alpha\rangle$ to first order in $|\mathbf{p}|$. This is simply

$$\begin{aligned}
H |\boldsymbol{\Gamma} + \mathbf{p}, \alpha\rangle &= -t \sum_{j=1}^3 e^{-i\alpha\mathbf{p} \cdot R_{\zeta_j} \boldsymbol{\tau}} |\boldsymbol{\Gamma} + \mathbf{p}, -\alpha\rangle \\
&\approx -t \sum_{j=1}^3 (1 - i\alpha\mathbf{p} \cdot R_{\zeta_j} \boldsymbol{\tau}) |\boldsymbol{\Gamma} + \mathbf{p}, -\alpha\rangle \\
&= -3t |\boldsymbol{\Gamma} + \mathbf{p}, -\alpha\rangle.
\end{aligned} \tag{S18}$$

B. With Kekulé-O distortion

We now consider the general case in which s and t may be different, so we are only guaranteed that the model is symmetric under translation by elements of L^{Kek} . When $s \neq t$, the system has lattice constant $a\sqrt{3}$. It is convenient to enumerate the lattice sites as $\mathbf{r} + \alpha R_{\zeta_j} \boldsymbol{\tau}$ for $\mathbf{r} \in L^{\text{Kek}}$, $\alpha \in \{+, -\}$, and $j \in \{1, 2, 3\}$, where $\boldsymbol{\tau}$ is given by Eq. (S9). As in Sec. II A, the A and B sublattices are defined by $\alpha = +$ and $\alpha = -$, respectively. We denote the orbital at site $\mathbf{r} + \alpha R_{\zeta_j} \boldsymbol{\tau}$ by $|\mathbf{r}, \alpha, j\rangle$ and define Bloch states

$$|\mathbf{k}, \alpha, j\rangle = \frac{1}{\sqrt{|BZ^{\text{Kek}}|}} \sum_{\mathbf{r} \in L^{\text{Kek}}} e^{i\mathbf{k} \cdot (\mathbf{r} + \alpha R_{\zeta_j} \boldsymbol{\tau})} |\mathbf{r}, \alpha, j\rangle. \tag{S19}$$

These Bloch states carry a corepresentation of $P6mm1'$ determined by

$$\begin{aligned}
T_{\mathbf{R}} |\mathbf{k}, \alpha, j\rangle &= e^{-i\mathbf{k} \cdot \mathbf{R}} |\mathbf{k}, \alpha, j\rangle, \\
C_{3z} |\mathbf{k}, \alpha, j\rangle &= |R_{2\pi/3} \mathbf{k}, \alpha, j+1\rangle, \\
M_x |\mathbf{k}, \alpha, j\rangle &= |\mathcal{R}_{\hat{\mathbf{x}}} \mathbf{k}, \alpha, 2-j\rangle, \\
M_y |\mathbf{k}, \alpha, j\rangle &= |\mathcal{R}_{\hat{\mathbf{y}}} \mathbf{k}, -\alpha, 2-j\rangle, \\
\mathcal{T} |\mathbf{k}, \alpha, j\rangle &= |-\mathbf{k}, \alpha, j\rangle,
\end{aligned} \tag{S20}$$

where $T_{\mathbf{R}}$ now denotes translation by $\mathbf{R} \in L^{\text{Kek}}$, and the j indices are defined modulo 3. The Hamiltonian commutes with the operators in Eq. (S20) and takes the form

$$H^{\text{Kek}} |\mathbf{k}, \alpha, j\rangle = -s e^{-i\alpha\mathbf{k} \cdot R_{\zeta_j} \boldsymbol{\tau}} |\mathbf{k}, -\alpha, j\rangle - t \sum_{j' \neq j} e^{i\alpha\mathbf{k} \cdot (R_{\zeta_j} + R_{\zeta_{j'}}) \boldsymbol{\tau}} |\mathbf{k}, -\alpha, j'\rangle. \tag{S21}$$

As illustrated in Fig. S1(a), the terms proportional to $-s$ and $-t$ produce hopping between and within the hexagons bounded by thick red lines, respectively.

As shown in Fig. S1(d), when s differs slightly from t the low energy physics for the Hamiltonian in Eq. (S21) consists of two gapped Dirac cones at the Γ^{Kek} point. To investigate this analytically, we first note that the Bloch states in Eqs. (S10) and (S19) are related by

$$|\mathbf{k}, \alpha\rangle = \frac{1}{\sqrt{3}} \sum_{j=1}^3 |\mathbf{k}, \alpha, j\rangle \quad (\text{S22})$$

and additionally the Bloch states in Eq. (S19) satisfy

$$|\mathbf{k} + \mathbf{G}, \alpha, j\rangle = e^{i\alpha\mathbf{G}\cdot\mathbf{R}_{\zeta_j}\boldsymbol{\tau}} |\mathbf{k}, \alpha, j\rangle \quad (\text{S23})$$

for $\mathbf{G} \in P^{\text{Kek}}$. Recalling that $\eta\mathbf{K} \in P^{\text{Kek}}$ for $\eta \in \{+, 0, -\}$ and using Eq. (S14), we then have

$$|\eta\mathbf{K} + \mathbf{p}, \alpha\rangle = \frac{1}{\sqrt{3}} \sum_{j=1}^3 e^{-i\eta\alpha\zeta_j} |\Gamma^{\text{Kek}} + \mathbf{p}, \alpha, j\rangle, \quad (\text{S24})$$

so that the states $|\eta\mathbf{K} + \mathbf{p}, \alpha\rangle$ and $|\Gamma^{\text{Kek}} + \mathbf{p}, \alpha, j\rangle$ for $\eta \in \{+, 0, -\}$ and $j \in \{1, 2, 3\}$ are related by a unitary change of basis. We can therefore study the low energy physics of H^{Kek} near the Γ^{Kek} point by expanding $H^{\text{Kek}}|\eta\mathbf{K} + \mathbf{p}, \alpha\rangle$ to first order in $|\mathbf{p}|$. Using the fact that the Hamiltonians in Eqs. (S12) and (S21) coincide when $s = t$, we have

$$\begin{aligned} (H^{\text{Kek}} - H) |\eta\mathbf{K} + \mathbf{p}, \alpha\rangle &= \frac{t-s}{\sqrt{3}} \sum_{j=1}^3 e^{-i\eta\alpha\zeta_j} e^{-i\alpha\mathbf{p}\cdot\mathbf{R}_{\zeta_j}\boldsymbol{\tau}} |\Gamma^{\text{Kek}} + \mathbf{p}, -\alpha, j\rangle \\ &= \frac{t-s}{3} \sum_{\eta' \in \{+, 0, -\}} \sum_{j=1}^3 e^{-i(\eta'+\eta)\alpha\zeta_j} e^{-i\alpha\mathbf{p}\cdot\mathbf{R}_{\zeta_j}\boldsymbol{\tau}} |\eta'\mathbf{K} + \mathbf{p}, -\alpha\rangle \end{aligned} \quad (\text{S25})$$

where H is given by Eq. (S12). Using Eqs. (S15) and (S18), for $\eta \neq 0$ we find

$$H^{\text{Kek}} |\eta\mathbf{K} + \mathbf{p}, \alpha\rangle \approx \hbar v_F^{\text{Kek}} \mathbf{p} \cdot (\eta\hat{\mathbf{x}} + i\alpha\hat{\mathbf{y}}) |\eta\mathbf{K} + \mathbf{p}, -\alpha\rangle + (t-s) |-\eta\mathbf{K} + \mathbf{p}, -\alpha\rangle + \hbar v_0 \mathbf{p} \cdot (-\eta\hat{\mathbf{x}} + i\alpha\hat{\mathbf{y}}) |\Gamma + \mathbf{p}, -\alpha\rangle \quad (\text{S26})$$

to first order in $|\mathbf{p}|$, where

$$v_F^{\text{Kek}} = \frac{s+2t}{3} \frac{a\sqrt{3}}{2\hbar}, \quad v_0 = \frac{s-t}{3} \frac{a\sqrt{3}}{2\hbar}. \quad (\text{S27})$$

Similarly, for $\eta = 0$ we find

$$H^{\text{Kek}} |\Gamma + \mathbf{p}, \alpha\rangle \approx -(s+2t) |\Gamma + \mathbf{p}, -\alpha\rangle + \sum_{\eta=\pm} \hbar v_0 \mathbf{p} \cdot (-\eta\hat{\mathbf{x}} + i\alpha\hat{\mathbf{y}}) |\eta\mathbf{K} + \mathbf{p}, -\alpha\rangle \quad (\text{S28})$$

to first order in $|\mathbf{p}|$.

C. Low energy continuum models

We assume that $|v_0/v_F^{\text{Kek}}|$ is small enough for us to treat perturbatively the terms in H^{Kek} coupling states near $\pm\mathbf{K}$ to states near Γ . Since these coupling terms are proportional to $|\mathbf{p}|$, they make no contribution to the low energy physics to first order in $|\mathbf{p}|$. The low energy physics for H^{Kek} near Γ^{Kek} is therefore described by the effective continuum Hamiltonian

$$H_0^{\text{Kek}} |\mathbf{p}, \eta, \alpha\rangle = \hbar v_F^{\text{Kek}} \mathbf{p} \cdot (\eta\hat{\mathbf{x}} + i\alpha\hat{\mathbf{y}}) |\mathbf{p}, \eta, -\alpha\rangle + m |\mathbf{p}, -\eta, -\alpha\rangle \quad (\text{S29})$$

where

$$m = t - s \quad (\text{S30})$$

and $|\mathbf{p}, \eta, \alpha\rangle$ for $\eta, \alpha \in \{+, -\}$ is a set of continuum states normalized by

$$\langle \mathbf{p}', \eta', \alpha' | \mathbf{p}, \eta, \alpha \rangle = \delta^2(\mathbf{p}' - \mathbf{p}) \delta_{\eta', \eta} \delta_{\alpha', \alpha}. \quad (\text{S31})$$

Defining the row vector of states

$$|\mathbf{p}\rangle = (|\mathbf{p}, +, +\rangle \quad |\mathbf{p}, +, -\rangle \quad |\mathbf{p}, -, +\rangle \quad |\mathbf{p}, -, -\rangle) \quad (\text{S32})$$

we can write

$$H_0^{\text{Kek}} = \int d^2\mathbf{p} |\mathbf{p}\rangle \mathcal{H}^{\text{Kek}}(\mathbf{p}) \langle \mathbf{p}| \quad (\text{S33})$$

$$\mathcal{H}^{\text{Kek}}(\mathbf{p}) = \begin{pmatrix} \hbar v_F^{\text{Kek}} \boldsymbol{\sigma} \cdot \mathbf{p} & m\sigma_x \\ m\sigma_x & -\hbar v_F^{\text{Kek}} \boldsymbol{\sigma}^* \cdot \mathbf{p} \end{pmatrix}.$$

In order to describe H_0^{Kek} in real space, we define real space continuum states

$$|\mathbf{r}, \eta, \alpha\rangle = \frac{1}{2\pi} \int d^2\mathbf{p} e^{-i\mathbf{p} \cdot \mathbf{r}} |\mathbf{p}, \eta, \alpha\rangle \quad (\text{S34})$$

which satisfy

$$\langle \mathbf{r}', \eta', \alpha' | \mathbf{r}, \eta, \alpha \rangle = \delta^2(\mathbf{r}' - \mathbf{r}) \delta_{\eta', \eta} \delta_{\alpha', \alpha}. \quad (\text{S35})$$

Defining the row vector of states

$$|\mathbf{r}\rangle = (|\mathbf{r}, +, +\rangle \quad |\mathbf{r}, +, -\rangle \quad |\mathbf{r}, -, +\rangle \quad |\mathbf{r}, -, -\rangle) \quad (\text{S36})$$

we can write

$$H_0^{\text{Kek}} = \int d^2\mathbf{r} |\mathbf{r}\rangle \mathcal{H}^{\text{Kek}}(\mathbf{r}) \langle \mathbf{r}| \quad (\text{S37})$$

$$\mathcal{H}^{\text{Kek}}(\mathbf{r}) = \begin{pmatrix} -i\hbar v_F^{\text{Kek}} \boldsymbol{\sigma} \cdot \nabla & m\sigma_x \\ m\sigma_x & i\hbar v_F^{\text{Kek}} \boldsymbol{\sigma}^* \cdot \nabla \end{pmatrix}.$$

In the special case that $s = t$, we have $m = 0$ and $v_F^{\text{Kek}} = v_F$ so that H_0^{Kek} simplifies to the continuum model H_0^{Gr} for graphene given by

$$H_0^{\text{Gr}} = \int d^2\mathbf{r} |\mathbf{r}\rangle \mathcal{H}^{\text{Gr}}(\mathbf{r}) \langle \mathbf{r}| \quad (\text{S38})$$

$$\mathcal{H}^{\text{Gr}}(\mathbf{r}) = \begin{pmatrix} -i\hbar v_F \boldsymbol{\sigma} \cdot \nabla & 0 \\ 0 & i\hbar v_F \boldsymbol{\sigma}^* \cdot \nabla \end{pmatrix}.$$

D. Spectrum and symmetry properties

We now consider the spectrum and symmetry properties of the continuum Hamiltonian H_0^{Kek} given by Eq. (S33). We first note that

$$U_0^\dagger \mathcal{H}^{\text{Kek}}(\mathbf{p}) U_0 = \begin{pmatrix} \hbar v_F^{\text{Kek}} \boldsymbol{\sigma} \cdot \mathbf{p} + m\sigma_z & 0 \\ 0 & -\hbar v_F^{\text{Kek}} \boldsymbol{\sigma}^* \cdot \mathbf{p} + m\sigma_z \end{pmatrix} \quad (\text{S39})$$

where

$$U_0 = \frac{1}{\sqrt{2}} \begin{pmatrix} \sigma_0 & -i\sigma_y \\ -i\sigma_y & \sigma_0 \end{pmatrix} \quad (\text{S40})$$

is a unitary matrix. As a result, the spectrum of H_0^{Kek} consists of two bands with dispersion $E_+(\mathbf{p})$ and two bands with dispersion $E_-(\mathbf{p})$ where

$$E_\pm(\mathbf{p}) = \pm \sqrt{(\hbar v_F^{\text{Kek}} |\mathbf{p}|)^2 + m^2}. \quad (\text{S41})$$

In particular, there is an energy gap of $2|m|$, as can be seen in Fig. S1(d).

Next, we note that H_0^{Kek} commutes with a corepresentation of the magnetic point group $6mm1'$ (see Appendix H of Ref. [28]) determined by

$$\begin{aligned} C_{3z} |\mathbf{p}\rangle &= |R_{2\pi/3}\mathbf{p}\rangle e^{i(2\pi/3)\sigma_z \otimes \sigma_z}, \\ M_x |\mathbf{p}\rangle &= |\mathcal{R}_{\hat{x}}\mathbf{p}\rangle \sigma_x \otimes \sigma_0, \\ M_y |\mathbf{p}\rangle &= |\mathcal{R}_{\hat{y}}\mathbf{p}\rangle \sigma_0 \otimes \sigma_x, \\ \mathcal{T} |\mathbf{p}\rangle &= |-\mathbf{p}\rangle \sigma_x \otimes \sigma_0. \end{aligned} \quad (\text{S42})$$

In accordance with Eq. (S32), the first and second tensor product factors here indicate valley and sublattice, respectively. The corepresentation in Eq. (S42) can be derived from Eq. (S11) under the identification of $|\mathbf{p}, \eta, \alpha\rangle$ with $|\eta\mathbf{K} + \mathbf{p}, \alpha\rangle$. To simplify this corepresentation, we take unitary change of basis

$$|\mathbf{p}\rangle' = |\mathbf{p}\rangle U_1, \quad U_1 = \frac{1}{\sqrt{2}} \begin{pmatrix} \sigma_x & -i\sigma_x \\ \sigma_0 & i\sigma_0 \end{pmatrix} \quad (\text{S43})$$

which mixes the valley and sublattice degrees of freedom. In this basis, the operators in Eq. (S42) become

$$\begin{aligned} C_{3z} |\mathbf{p}\rangle' &= |R_{2\pi/3}\mathbf{p}\rangle' e^{-i(2\pi/3)\sigma_z} \oplus e^{-i(2\pi/3)\sigma_z}, \\ M_x |\mathbf{p}\rangle' &= |\mathcal{R}_{\hat{x}}\mathbf{p}\rangle' \sigma_x \oplus (-\sigma_x), \\ M_y |\mathbf{p}\rangle' &= |\mathcal{R}_{\hat{y}}\mathbf{p}\rangle' \sigma_x \oplus \sigma_x, \\ \mathcal{T} |\mathbf{p}\rangle' &= |-\mathbf{p}\rangle' \sigma_x \oplus \sigma_x. \end{aligned} \quad (\text{S44})$$

At $\mathbf{p} = \mathbf{0}$, this corepresentation decomposes as the direct sum of two different 2D irreducible corepresentations which are called E_2 and E_1 (see Table III of Ref. [28]). In this basis, the Hamiltonian matrix becomes

$$U_1^\dagger \mathcal{H}^{\text{Kek}}(\mathbf{p}) U_1 = \begin{pmatrix} m\sigma_0 & -i\hbar v_F^{\text{Kek}} \boldsymbol{\sigma}^* \cdot \mathbf{p} \\ i\hbar v_F^{\text{Kek}} \boldsymbol{\sigma}^* \cdot \mathbf{p} & -m\sigma_0 \end{pmatrix} \quad (\text{S45})$$

which is diagonal when $\mathbf{p} = \mathbf{0}$.

III. COMPACT LOCALIZED STATES AND NONCONTRACTIBLE LOOP STATES

The tight-binding Hamiltonians in Eqs. (6) and (7) have exactly flat bands with symmetry protected band touchings at the Γ point [24–26, 28]. As explained in Ref. [44], the flat bands of such models can generally be spanned by a collection of compact localized states (CLSs) and noncontractible loop states (NLSs), all of which are eigenstates of the Hamiltonian with a fixed energy. As the names suggest, CLSs have compact support, while NLSs are compact in one direction, but span a noncontractible loop in the other direction, when the system is defined with periodic boundary conditions. In the following subsections, we construct the CLSs and NLSs for the flat bands in the Hamiltonians in Eqs. (6) and (7). In both cases, we assume the model is defined with periodic boundary conditions and a total of N_{tot} unit cells.

A. One-orbital kagome model

We first consider the one-orbital kagome lattice Hamiltonian H_{kag} in Eq. (7). Fig. S2(a) shows the band structure of H_{kag} , which has one exactly flat band with energy $-2t$. The CLSs and NLSs for this flat band were previously described in Refs. [26, 44], and we review them now. Fig. S2(b) illustrates a prototypical CLS, which is supported on a hexagon of sites shown in red. The coefficients are $+1$ and -1 in an alternating pattern, with signs shown in the figure. It is straightforward to check that such a state is an eigenstate of H_{kag} with energy $-2t$. Although there are N_{tot} such CLSs, the sum of all these states is zero. As a result, there are $N_{\text{tot}} - 1$ linearly independent CLSs.

Fig. S2(c),(d) illustrate two NLSs, which are supported on the noncontractible loops of sites shown in red. The coefficients are $+1$ and -1 in an alternating pattern, with signs shown in the figures. It is straightforward to check that these states are also eigenstates of H_{kag} with energy $-2t$. The $N_{\text{tot}} - 1$ CLSs and two NLSs form a basis for the flat band and its band touching.

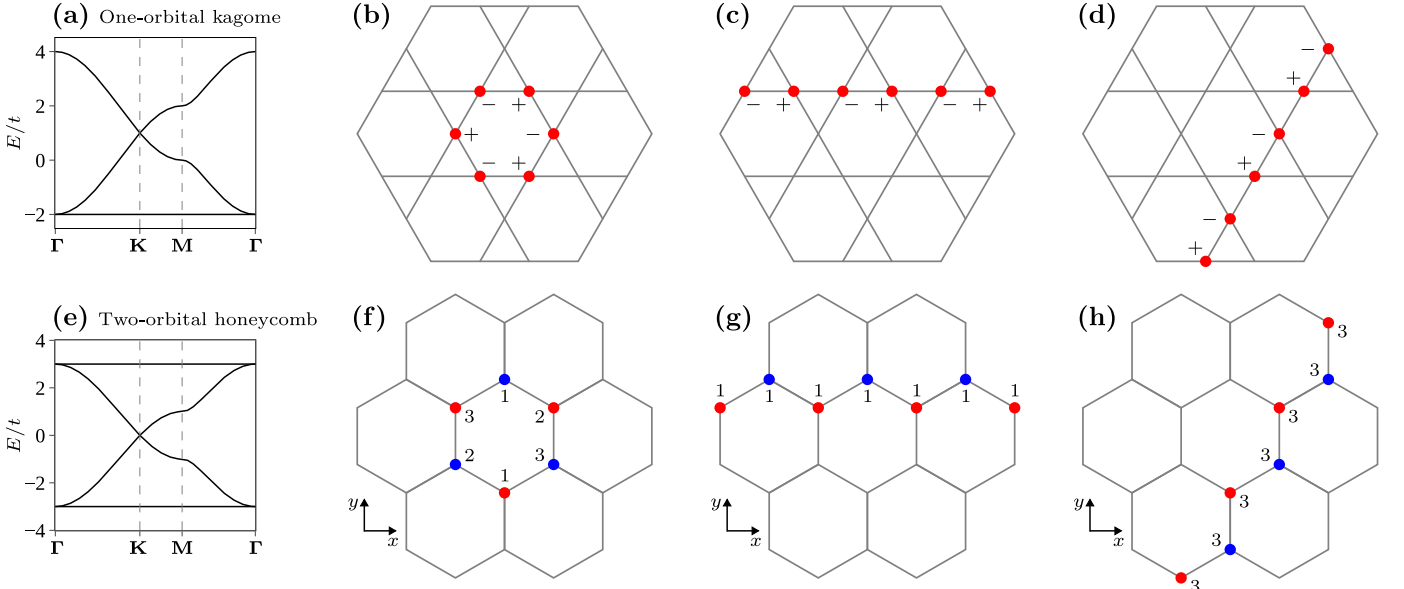


FIG. S2. (a) Band structure of the one-orbital kagome lattice Hamiltonian H_{kag} in Eq. (7). (b) Illustration of a prototypical compact localized state for H_{kag} . (c), (d) Illustrations of two noncontractible loop states for H_{kag} . (e) Band structure of the two-orbital honeycomb lattice Hamiltonian H_{hc} in Eq. (6), with $|t_+| = |t_-| = t$. (f) Illustration of a prototypical compact localized state for H_{hc} . (g), (h) Illustrations of two noncontractible loop states for H_{hc} .

B. Two-orbital honeycomb model

Next, we consider the two-orbital honeycomb lattice Hamiltonian H_{hc} in Eq. (6). H_{hc} has two exactly flat bands when $|t_+| = |t_-|$ [24, 25, 28]. However, the two cases $t_+ = t_-$ and $t_+ = -t_-$ are related by a sign reversal on the $\ell = -1$ orbitals. As a result, we can choose $t_+ = t_- = t$ without loss of generality. Similarly, changing the axis with respect to which the $\varphi_{j',j}$ angles are defined is equivalent to changing the phases of the orbitals. This implies that we lose no generality by defining $\varphi_{j',j}$ relative to the y axis shown in Fig. S2(f)-(h).

We indicate the two sublattices of the honeycomb lattice by blue and red colors in Fig. S2(f)-(h). We assign these sublattices the values $\alpha = +$ (blue) and $\alpha = -$ (red) and define C to be a diagonal operator whose entries are these sublattice values. Fig. S2(e) shows the band structure of H_{hc} , which has two exactly flat bands with energies $-3t$ and $3t$. In fact, the entire band structure is symmetric about energy 0 due to the anticommutation identity $\{H_{\text{hc}}, C\} = 0$. As a result, it suffices to find the CLSs and NLSs for the flat band with energy $-3t$, since the two flat bands are related by the C operator.

Fig. S2(f) illustrates a prototypical CLS, which is supported on a hexagon of sites colored blue and red. Each site carries an integer label, and the coefficient for the ℓ orbital on a site with label n is $\ell e^{-i\ell\zeta_n}$ where $\zeta_n = \frac{2\pi}{3}(n-1)$. The coefficients do not depend on sublattice. We now check that this CLS is indeed an eigenstate of H_{hc} with energy $-3t$. To do so, we compute the amplitude on a state $|j', \ell'\rangle$ after H_{hc} is applied to the CLS. If j' is neither in the CLS nor is a nearest neighbor of a site in the CLS, then the amplitude is zero. Next, suppose that j' is not in the CLS, but is a nearest neighbor of a site in the CLS with label n . The amplitude is then

$$t \sum_{\ell=\pm 1} e^{i(\ell-\ell')\zeta_n} \ell e^{-i\ell\zeta_n} = t e^{-i\ell'\zeta_n} \sum_{\ell=\pm 1} \ell = 0. \quad (\text{S46})$$

Finally, suppose that j' is in the CLS and has label n' . The amplitude is then

$$\begin{aligned} t \sum_{\ell=\pm 1} \sum_{\substack{1 \leq n \leq 3 \\ n \neq n'}} e^{i(\ell-\ell')(2\pi-\zeta_n-\zeta_{n'})} \ell e^{-i\ell\zeta_n} &= t \sum_{\substack{1 \leq n \leq 3 \\ n \neq n'}} \ell' e^{-i\ell'\zeta_n} + e^{-i\ell'(\zeta_n+\zeta_{n'})} (-\ell') e^{i\ell'\zeta_n} \\ &= t \ell' \sum_{\substack{1 \leq n \leq 3 \\ n \neq n'}} e^{-i\ell'\zeta_n} - e^{-i\ell'\zeta_{n'}} \\ &= -3t \left(\ell' e^{-i\ell'\zeta_{n'}} \right). \end{aligned} \quad (\text{S47})$$

We conclude that the CLS shown in Fig. S2(f) is indeed an eigenstate of H_{hc} with energy $-3t$. Although there are N_{tot} CLSs of the form shown in Fig. S2(f), the sum of all these states is zero. As a result, there are $N_{\text{tot}} - 1$ linearly independent CLSs.

Fig. S2(g),(h) illustrate two NLSs, which are supported on the noncontractible loops of sites colored blue and red. Each site carries an integer label, and in either NLS the coefficient for the ℓ orbital on a site of sublattice α and label n is $\alpha \ell e^{-i\ell\zeta_n}$ where $\zeta_n = \frac{2\pi}{3}(n-1)$. We now check that these NLSs are indeed eigenstates of H_{hc} with energy $-3t$. To do so, we compute the amplitude on a state $|j', \ell'\rangle$ after H_{hc} is applied to an NLS. If j' is neither in the NLS nor is a nearest neighbor of a site in the NLS, then the amplitude is zero. Next, suppose that j' is not in the NLS, but is a nearest neighbor of a site in the NLS with sublattice α and label n . The amplitude is then

$$t \sum_{\ell=\pm 1} e^{i(\ell-\ell')\zeta_n} \alpha \ell e^{-i\ell\zeta_n} = t\alpha e^{-i\ell'\zeta_n} \sum_{\ell=\pm 1} \ell = 0. \quad (\text{S48})$$

Finally, suppose that j' is in the CLS and has sublattice α' and label n' . The amplitude is then

$$\begin{aligned} t \sum_{\ell=\pm 1} \sum_{\substack{1 \leq n \leq 3 \\ n \neq n'}} e^{i(\ell-\ell')\zeta_n} (-\alpha') \ell e^{-i\ell\zeta_n} &= -t\alpha' \sum_{\substack{1 \leq n \leq 3 \\ n \neq n'}} \ell' e^{-i\ell'\zeta_{n'}} + e^{i\ell'\zeta_{n'}} (-\ell') e^{i\ell'\zeta_{n'}} \\ &= -t\alpha' \ell' \left(2e^{-i\ell'\zeta_{n'}} - e^{i\ell'\zeta_{n'}} \sum_{\substack{1 \leq n \leq 3 \\ n \neq n'}} e^{i\ell'\zeta_n} \right) \\ &= -3t(\alpha' \ell' e^{-i\ell'\zeta_{n'}}). \end{aligned} \quad (\text{S49})$$

We conclude that the NLSs shown in Fig. S2(g),(h) are indeed eigenstates of H_{hc} with energy $-3t$. The $N_{\text{tot}} - 1$ CLSs and two NLSs form a basis for the flat band of energy $-3t$ and its band touching.

IV. PARAMETER VARIATION

We now discuss the effects of parameter variation on the band structures of TGKG and TBKG. Figs. S3 and S4 show variations on the band structures in Fig. 2, with one parameter varied in each panel. We see that the structure of the two-orbital honeycomb bands in TGKG is quite sensitive to w_0/w_1 , ϵ , m_+ and θ , but is relatively insensitive to E_Δ . In each case, the two-orbital honeycomb bands remain isolated. On the other hand, the structure of the one-orbital kagome bands in TBKG is quite insensitive to all parameters considered, but the bands are no longer isolated in Fig. S4(f).

Fig. S5(a) shows the bandwidth of the $n = \pm 2$ two-orbital honeycomb lattice flat bands in TGKG as a function of θ and m_+ , as in Fig. 3(a), except that we now take $w_0/w_1 = 0.7$. We see that upon changing the value of w_0/w_1 , the magic TGKG regime moves near $\theta = 0.65^\circ$, $m_+ = 120$ meV. Fig. S5(e) shows the band structure with these modified magic parameters, which exhibits a two-orbital honeycomb lattice flat band model.

Similarly, Fig. S5(b) is identical to Fig. 3(a), except that we now take $\epsilon = -0.01$. In this case, we do not observe a magic TGKG regime. Fig. S5(c),(d) are identical to Fig. 3(b) except that $w_0/w_1 = 0.7$ in Fig. S5(c) and $\epsilon = -0.01$ in Fig. S5(d). Both of these plots indicate the presence of flat one-orbital kagome bands in a large parameter regime.

It is worth noting that the results in Refs. [32, 34] which experimentally realize Kekulé-O graphene are consistent with $\epsilon = 0$. For a theoretical justification of the small magnitude of ϵ , one can consult DFT calculations of lithium intercalated graphene. For example, the results in Ref. [52] with density functional vdW-optPBE produce $\epsilon \approx -0.01$.

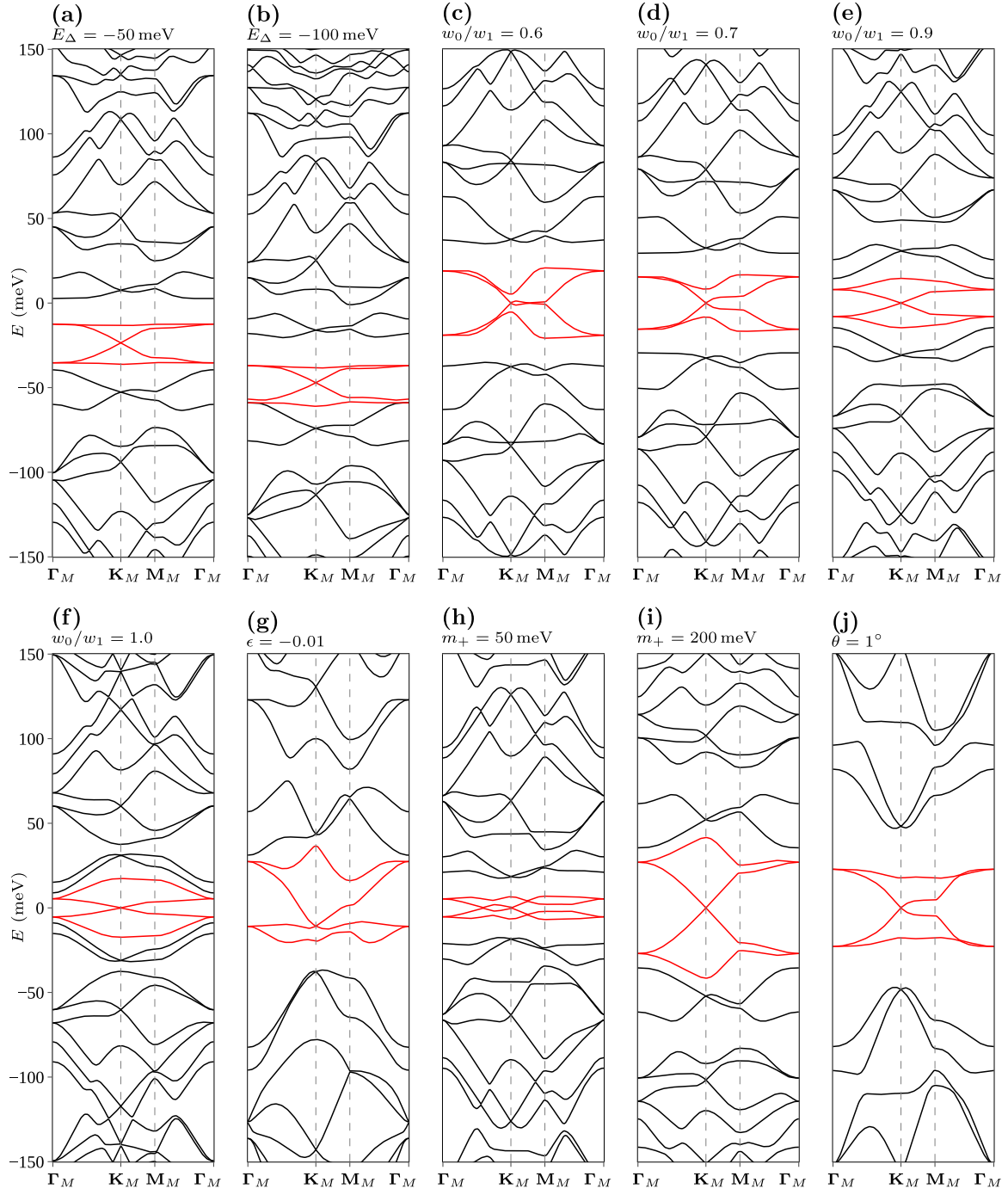


FIG. S3. Variations on the TGKG band structure in Fig. 2(a). In each panel, all parameters are fixed at those used in Fig. 2(a) except as indicated. Bands $-2 \leq n \leq 2$ are shown in red. Except in (b), these bands always form an isolated honeycomb lattice model with EBCR $(^1E^2E)_{2b}$ of $P61'$. In (b), bands $-1 \leq n \leq 2$ and $-4 \leq n \leq -2$ correspond to EBCRs $(^1E_1^2E_1)_{1a} \oplus (B)_{1a}$ and $(^1E_2^2E_2)_{1a} \oplus (A)_{1a}$ of $P61'$, respectively, and are therefore triangular lattice models.

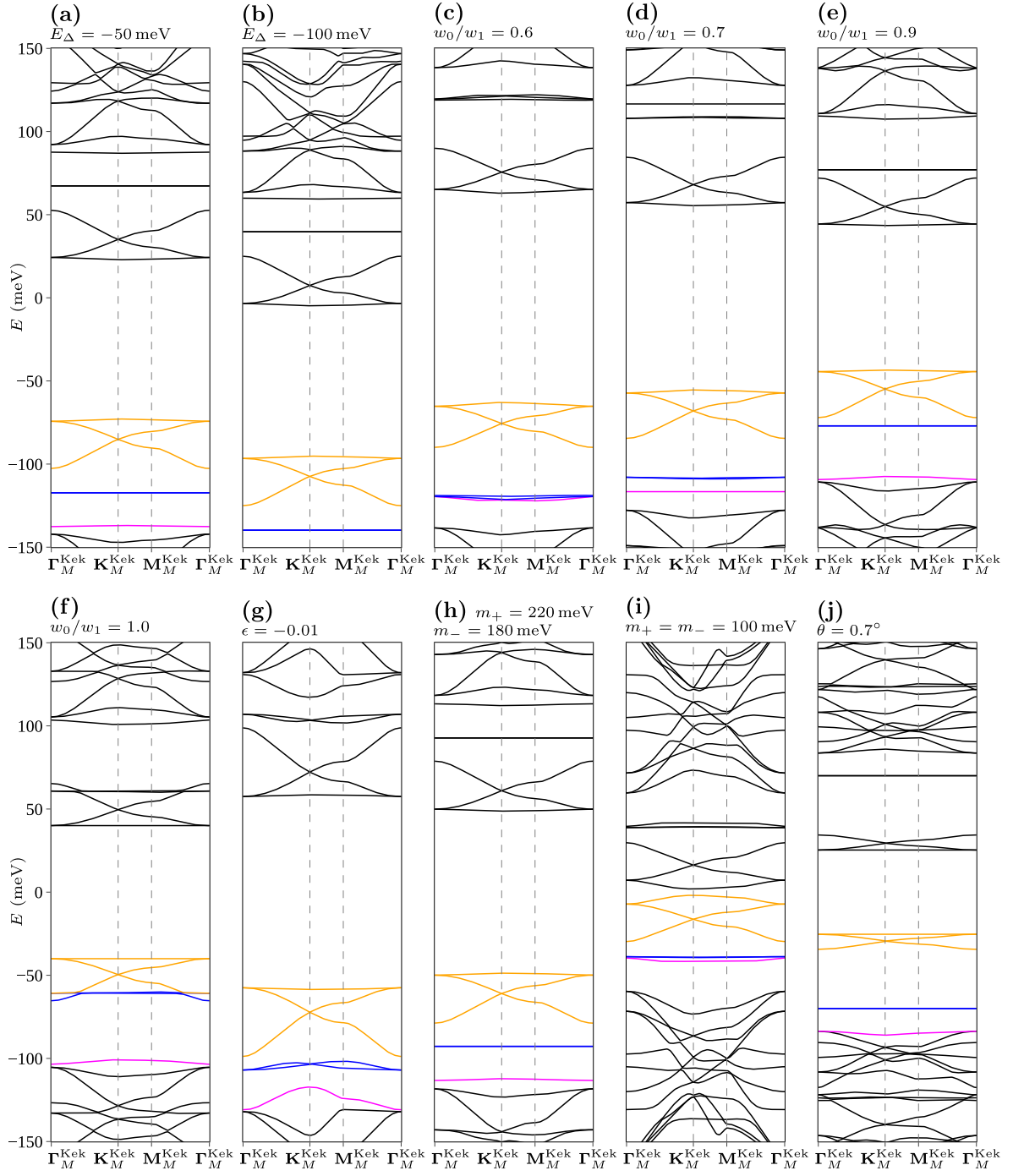


FIG. S4. Variations on the TBKG band structure in Fig. 2(b). In each panel, all parameters are fixed at those used in Fig. 2(b) except as indicated. Bands $-3 \leq n \leq -1$ are shown in orange, bands $-5 \leq n \leq -4$ are shown in blue, and band $n = -6$ is shown in magenta. Except in (f), bands $-3 \leq n \leq -1$ and $1 \leq n \leq 3$ always form isolated kagome lattice flat band models with EBCRs $(B)_{3c}$ and $(A)_{3c}$ of $P61'$, respectively. In (f), bands $n = \pm 1$ are still extremely flat and bands $-4 \leq n \leq -1$ and $1 \leq n \leq 4$ correspond to EBCRs $(B)_{3c} \oplus ({}^1E_2 {}^2E_2)_{1a}$ and $(A)_{3c} \oplus ({}^1E_1 {}^2E_1)_{1a}$ of $P61'$, respectively.

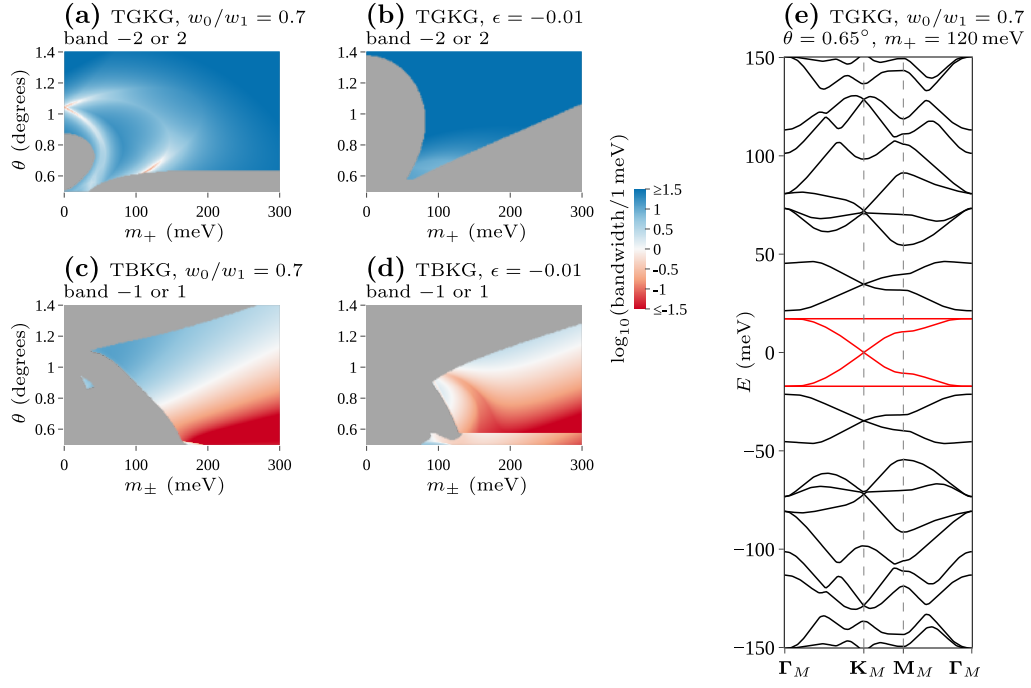


FIG. S5. (a), (b) Variations on the plots in Fig. 3(a). (c), (d) Variations on the plots in Fig. 3(b). In each panel, all parameters are fixed at those used in Fig. 3 except for w_0/w_1 or ϵ , as indicated. (e) Band structure of TGKG with $w_0/w_1 = 0.7$ and the modified magic parameters $\theta = 0.65^\circ$ and $m_+ = 120 \text{ meV}$ from (a).